HIGH ENERGY HADRON PHYSICS WITH THE FNAL HYBRID BUBBLE CHAMBER SYSTEM

Richard K. YAMAMOTO
Massachusetts Institute of Technology
Cambridge, Massachusetts, U. S. A.

Contents

INTRODUCTION

It seems that the study of multiparticle production in hadronic collisions is by far the most difficult to undertake since it deals with many degrees of freedom in the initial as well as final states. The trend in the study of hadronic interactions is toward that for small cross section processes where again only a few degrees of freedom are involved, i.e., single quark-quark interactions such as Drell-Yan processes, etc. However, with the continuing development of Quantum Chromo-Dynamics, it would hopefully be only a matter of short time before we again must study the large cross section multi-hadronic productions which in principle a successful QCD theory should be able to deal with.

Although much of what I will discuss deals with higher energies, the parameterization and ideas, for the most part, are applicable at KEK energies. I have a strong feeling that much more systematic work dealing with hadronic interactions can be done at KEK. This is an energy regime which much of your Western colleagues had to abandon in order to join the ultra-high energy research. Most of what happens in strong interactions happen at lower energies, and yet we really cannot explain why, in detail. The fact that new particles are discovered at higher energies have not really told us much more about the "every day" pions, kaons, and the like that are copiously produced at lower energies. Could it be that the ultra-high energy accelerators were built too soon? The answer may lie in Ibaraki-ken.

I will discuss only a few of the many aspects of hadron physics at high energies. The lectures will cover three main areas:

1) A brief general review of the kinematic variables and some of the language used in this field.

2) A short description of the Fermilab Hybrid Spectrometer and some of its characteristics.

3) Discussion of some results obtained from the Hybrid Spectrometer at $\sim$ 150 GeV.

Due to the limited time available, these discussions will necessarily be brief and I will not discuss much of the work carried out in this field by other workers but refer you to refs. 1-3 and all the references contained therein. The purpose of these discussions are meant to be educational for the novice and therefore may seem trite for the experienced.

I. KINEMATIC VARIABLES AND THE PICTURES THEY HELP TO DESCRIBE.

A. Variables

Much of what will be described here is ten or more years old and can be found in the literature[4-7]. Although somewhat archaic and not in the contemporary language of QCD, much of what follows is model independent and forms a good mnemonic for the general description of hadronic interactions.

Two basic facts underlie hadronic interactions, at least in the gross sense:

1) The transverse momentum of particles produced in an interaction are limited. $\langle P_T \rangle \sim 0.3 - 0.4$ GeV/c, independent of interaction energy.

2) The number of particles produced in an interaction is far less than possible from the available energy.

$$\langle n \rangle << \frac{\sqrt{s}}{M}$$

where $\langle n \rangle$ is the average number of particles produced in an event, $\sqrt{s}$ is the energy available in the C. M. S. and M is the average mass of a particle. In fact

$$\langle n \rangle \sim A + B \ln s$$

(this is an empirical statement and can be shown to be a consequence of scaling and finite correlation length - see section IIC).

Due to these two facts of hadronic nature, the longitudinal momentum, P_{11}, of particles produced in an interaction plays a key role in describing an event. Another way of stating this is that in phase space, that

region determined by P_{11} is of greatest importance. A second consequence of facts 1) and 2) is that the average longitudinal momentum P_{11} increases very rapidly with available energy s. This is easily seen from the following:

$$\langle P_T \rangle^2 + \langle P_{11}^* \rangle^2 \sim \frac{s}{\langle n \rangle^2} \sim \frac{s}{(\ln s)^2} \qquad \text{(I-1)}$$

P_{11}^* = longitudinal momentum in C.M.S.

but since $\langle P_T \rangle^2$ is constant and independent of s (fact 1),

$$\langle P_{11}^* \rangle^2 \sim \frac{s}{(\ln s)^2} - \text{const} \rightarrow \langle P_{11}^* \rangle \sim \frac{\sqrt{s}}{\ln s} \qquad \text{(I-2)}$$

Unfortunately, because of this nature, some of the particles produced in an interaction are very difficult to detect and measure in the laboratory since their production angle

$$\theta \sim \frac{P_T}{P_{11}} \xrightarrow[s \rightarrow \text{large}]{} 0 \qquad \text{(I-3)}$$

One advantage of the Hybrid System is a remedy to this problem, as is discussed in Section IIB.

Techniques to emphasize the longitudinal momentum region of phase space have been devised and in particular the Longitudinal Phase Space (LPS) plot of Van Hove[8] and the Prism Plot analysis of Pless[9] have been very useful at lower energies. However, as one goes to higher energies, the multiplicity of particles in an event increases, albeit slowly, to a level where such plots become difficult to display, especially for events with more than four observed particles. At this point, the notion of single particle measurements, inclusive of all final states ("inclusive" measurements) as opposed to complete measurements of specific final states, exclusive of all other final states ("exclusive" measurements) become very useful. This is especially true from the standpoint of experiment since the simultaneous precision measurement of several closely grouped particles (see I-3) becomes difficult. On the other hand, much information is sacrificed in inclusive measurements.

What variables should one use? The basic Lorentz invariant single particle spectrum is given by:

$$E \frac{d\sigma}{d\vec{P}} = F(\vec{P}, E, s) \tag{I-4}$$

where E is the energy of the particle, $\vec{P}$ its momentum and s the square of the interaction energy in the C. M. S.

Since the longitudinal momentum plays such a dominant role, it is best to represent (I-4) in terms of some variable representative of P_{11}. Toward this end, several variables have come into vogue and of these we will mention the rapidity variable y and the Feynman scaling variable x.

The rapidity variable y has long been known to cosmic ray physicists but more recently revived and applied in hadronic studies[10,11,5]. It is defined for a single particle as:

$$y = \frac{1}{2} \ln \frac{E + P_{11}}{E - P_{11}} \tag{I-5}$$

$$E^2 = P_{11}^2 + P_T^2 + \mu^2 \tag{I-6}$$

where E is the energy of the particle with mass μ and components of momentum longitudinal (P_{11}) and transverse (P_T) to a given axis, i.e., the z axis. This implies:

$$\sinh y = \frac{P_{11}}{E_T} \tag{I-7a}$$

$$\cosh y = \frac{E}{E_T} \tag{I-7b}$$

$$E_T \equiv \sqrt{P_T^2 + \mu^2} \tag{I-8}$$

The 4-vector of a particle is then:

$$P = (E, P_x, P_y, P_z) = (E_T \cosh y, P_x, P_y, E_T \sinh y)$$

where we have chosen $P_z = P_{11}$.

A nice feature of the rapidity variable is that a Lorentz boost along the z direction results in a simple transformation where the new y variable is different from the old only by an additive constant. This follows from:

$$P_{11} = \gamma (P'_{11} + \beta E') \tag{I-9}$$

$$\left.\begin{aligned} P_x &= P'_x \\ P_y &= P'_y \end{aligned}\right\} \rightarrow E_T = E'_T \tag{I-10}$$

$$E = \gamma (E' + \beta P'_{11}) \tag{I-11}$$

$$\therefore \quad \begin{aligned} E_T \sinh y &= \gamma (E_T \sinh y' + \beta E_T \cosh y') \\ E_T \cosh y &= \gamma (E_T \cosh y' + \beta E_T \sinh y') \end{aligned}$$

from which follows

$$e^y = \gamma (1 + \beta) e^{y'} = \left(\frac{1 + \beta}{1 - \beta}\right)^{\frac{1}{2}} e^{y'}$$

$$\therefore \quad y = y' + \frac{1}{2} \ln \left(\frac{1 + \beta}{1 - \beta}\right) \equiv y' + u \tag{I-12}$$

where $\cosh u = \gamma$ depends only on the boost parameters.

Thus $dy = dy'$ and therefore distributions of y are invariant in shape and only displaced when a Lorentz transformation from one reference frame to another is performed along the z axis.

Other relations follow easily. Consider the laboratory frame:

$$P_{\text{projectile}} \equiv P_p = (\mu_p \cosh y_p, 0, 0, \mu_p \sinh y_p)$$

$$P_{\text{target}} \equiv P_t = (\mu_t, 0, 0, 0)$$

then $s = (P_p + P_t)^2 = \mu_p^2 + \mu_t^2 + 2\mu_p\mu_t \cosh y_p$ and for y_p large,

$$S \sim \mu_p \mu_t e^{y_p} \tag{I-13}$$

Since $y_t = 0$, the range of y possible for a particle is:

$$\Delta_y = y_p - y_t = y_p \sim \ln \frac{s}{\mu_p \mu_t} \tag{I-14}$$

Another variable x, introduced by Feynman[12,13] is defined as

$$x \equiv \frac{P^*_{11}}{P^*_{\text{max}}} \tag{I-15}$$

which is the ratio of the longitudinal momentum to the maximum possible momentum in the C. M. S. For high energies,

$$x \sim \frac{2P^*_{11}}{\sqrt{s}} \qquad \text{(I-16)}$$

In terms of y^*, x can be written as

$$x = e^{y^* - \Delta y/2} - e^{-(y^* + \Delta y/2)}$$

The choice in use of these variables depends mainly on convenience and the nature of what is being studied.

Considering cross sections, the invariant spectrum

$$E\frac{d\sigma}{d\vec{P}} = \frac{d\sigma}{dyd\vec{P}_T} = \frac{d\sigma}{\pi dyd(P_T^2)} \qquad \text{(I-17)}$$

since $dy = \frac{dP_{11}}{E}$ for fixed P_T.

$$\text{Also, } E\frac{d\sigma}{d\vec{P}} = E^*\frac{d\sigma}{d\vec{P}^*} = \frac{2E^* d\sigma}{\pi\sqrt{s}dxd(P_T^2)} \qquad \text{(I-18)}$$

$$\text{since } \frac{dP^*_{11}}{E^*} = \frac{\sqrt{s}dx}{2E^*}, \quad x \equiv \frac{2P^*_{11}}{\sqrt{s}}.$$

B. Limiting Fragmentation and Scaling

The notion of "limiting fragmentation"[14] states that in the laboratory frame (fixed target experiment):

$$E\frac{d\sigma}{d\vec{P}}(P_{11}, P_T, s) \xrightarrow[s \to \infty]{} E\frac{d\sigma}{d\vec{P}}(P_{11}, P_T) \qquad \text{(I-19)}$$

In other words, the single particle cross section becomes independent of s as it approaches infinity. In particular this implies that for finite but large s and fixed P_{11} and P_T, the particles should display the same momentum spectra independent of s. These particles would be of low momentum in the laboratory and thus correspond to target fragments. (see Fig. 1) On the other hand, if one makes the observation in the rest frame of the projectile a similar statement can be made where the projectile fragments would display momentum spectra independent of s.

Thus in the limit of large s both the target and projectile fragments should display spectra in their corresponding frames that are independent of s. This is a form of scaling in the kinematic regions pertaining to the target and projectile. What about regions not pertaining to either target or projectile?

Feynman[12] has argued from the "parton" picture that the particle spectrum

$$E\frac{d\sigma}{d\vec{P}}(P^*_{11}, P_T, s) \xrightarrow[s \to \infty]{} E\frac{d\sigma}{d\vec{P}}(x, P_T) \qquad \text{(I-20)}$$

This relation states that as s increases, the single particle spectrum will ultimately depend only on the transverse component of momentum and the scale variable $x = \frac{2P^*_{11}}{\sqrt{s}}$. For values of $x >> 2E_T/\sqrt{s}$ relation (I-20) is equivalent to limiting fragmentation in the projectile region whereas for $x << -2E_T/\sqrt{s}$ it is equivalent to limiting fragmentation in the target region. This is evident from the fact that

$$x \sim (P_{11} + E)/\mu_p \text{ in the projectile rest frame for } x >> 2E_T/\sqrt{s}$$

and

$$x \sim (P_{11} - E)/\mu_t \text{ in the target rest frame for } x << -2E_T/\sqrt{s}$$

Thus Feynman scaling (I-20) is consistent with limiting fragmentation and therefore is a somewhat more general statement than the hypothesis of limiting fragmentation which deals with scaling only in the fragmentation regions.

Evidence for Feynman scaling can be seen in the P-P data from the CERN-ISR for various inclusive single particle measurements[3]. These are shown in Figures 2-6 which display x spectra for fixed P_T, and P_T spectra for fixed x, for $K^\pm$, $\pi^\pm$, $P^\pm$ from s = 551 to 2800 GeV^2. The bubble chamber data[2] in Figure 7 displays Feynman scaling, at least in the proton target hemisphere, from $s \sim 33$ to ~ 200 GeV^2.

C. The Finite Correlation Length Hypothesis

Another aspect of multiparticle production is the hypothesis that there exists a fundamental "distance" between two particles in phase space beyond which the particles behave independently of each other. This is usually refered to as the correlation length hypothesis[4, 5]. Given this hypothesis, much can be said about the general nature of hadronic interactions.

In the inclusive reaction

$$a_{proj} + b_{targ} \to c + X \qquad X = \text{any other particles} \tag{I-21}$$

one would expect the rapidity spectrum of particle c to have some form, such as the solid curve in Figure 8. The rapidity range allowed for particle c is $y_a - y_b \sim \ln\frac{s}{\mu_a \mu_b}$. Consider two particles of type c in a given event with rapidity values y_{c_1} and y_{c_2}. The hypothesis of finite correlation length then states that for $|y_{c_2} - y_{c_1}| \gg L$ there is no inter-dependence between c_1 and c_2. L is some value governed by the dynamics of the interaction. Consequently, if for a single particle c, $|y_{a,b} - y_c| < L$, then the behavior of c should not depend on the nature of either the target b or projectile a. Furthermore, if $|y_{c_1} - y_{c_2}| \gg L$, the behavior of c_1 should not depend on the nature of c_2, and vice versa. Conversely, if $|y_{c_1} - y_{c_2}| < L$, there may be an inter-dependence between c_1 and c_2 on their nature as well as kinematically. This latter statement leads to the notion of local compensation of quantum numbers, which is discussed in section IIIC.

Given the hypothesis of finite correlation length and scaling, can we say anything further? The answer is yes. We can argue that the rapidity spectrum should display a "plateau" or constant region as shown by the dashed curve in Figure 8, if $|y_a - y_b| \gg 2L$. The argument goes as follows.

Limiting fragmentation predicts

$$\frac{d\sigma}{\pi dy d(P_T^2)} \sim F(y - y_a, P_T) \text{ independent of } s \tag{I-22}$$

for $y_a > y > y_a - L$ (projectile region)

and

$$\frac{d\sigma}{\pi dy d(P_T^2)} \sim F(y_b - y, P_T) \tag{I-23}$$

for $y_b + L > y > y_b$ (target region).

The hypothesis of finite correlation length then states for $y < y_a - L$, (I-22) should not depend on the nature of the projectile and likewise for $y > y_b + L$ (I-23) should be independent of the nature of the target. Thus in this "central region", $y_b + L < y < y_a - L$,

$$\frac{d\sigma}{\pi dy d(P_T^2)} \sim F(P_T) \tag{I-24}$$

and the spectrum is independent of y. This leads to the plateau depicted in Figure 8, which is an underlying feature of multiperipheral models (see ref. 5). Experimental evidence for a rapidity plateau can clearly be seen in the ISR data[3] shown in Figure 9. These distributions were measured at fixed $P_T = 0.4$ GeV/c for the various single particles produced.

We can also show that the average number of particles of type c produced in an event, $\langle n_c \rangle$, has a ln s behavior. The average is given by:

$$\langle n_c \rangle = \frac{1}{\sigma} \int \frac{d\sigma^c}{dy d(P_T^2)} dy d(P_T^2) \tag{I-25}$$

This follows from the fact that the integral includes the count n_c of particles of type c, produced in an event. The total cross section $\sigma = \sum_c \sigma^c$.

$$\langle n_c \rangle = \frac{1}{\sigma} \Big[\underbrace{\int \frac{d\sigma^c}{dy d(P_T^2)} \cdot dy d(P_T^2)}_{\text{Proj. region}} + \underbrace{\int \frac{d\sigma^c}{dy d(P_T^2)} \cdot dy d(P_T^2)}_{\text{Targ. region}} + \underbrace{\int \frac{d\sigma^c}{dy d(P_T^2)} \cdot dy d(P_T^2)}_{\text{Central region}} \Big] \tag{I-26}$$

The first two integrals represent contributions dependent on projectile and target particle types whereas the third integral is not and in fact from (I-24) we see that it is simply a constant multiplied by the width of the central region.

$$\int_{\text{Central region}} \frac{d\sigma^c}{dy\,d(P_T^2)}\, dy\,d(P_T^2) = \int_{\text{Central region}} F^c(P_T)\,dy\,d(P_T^2) = C' \int_{\text{Central region}} dy$$

We can estimate $\Delta y_{\text{Central region}}$ from (I-14)

$$\Delta y_{\text{Central region}} \sim \ln \frac{s}{\mu_a \mu_b} - 2L$$

$$\therefore \quad \langle n_c \rangle = \frac{1}{\sigma} [A'_{proj} + B'_{targ} + C' \ln s] \text{ or}$$

$$\langle n_c \rangle = A_{proj} + B_{targ} + C \ln s \qquad \text{(I-27)}$$

This ln s dependence of $\langle n_c \rangle$ is an observed fact. More of this will be discussed in section IIIB.

D. Mueller - Regge Analysis

Mueller[15,16] has shown that the generalized optical theorem can accommodate the cross section calculations for inclusive processes. The details will not be described here but only some results will be stated.

The optical theorem states that the cross section for a two body interaction

$a + b \to X$ (anything)

is related to the imaginary part (discontinuity in s) of the forward scattering amplitude for

$a + b \to a + b$

(see Figure 10).

For the single particle inclusive reaction

$a + b \to c + X$

the generalized optical theorem then relates the cross section to the discontinuity in M^2 of the amplitude for

$a + b + \bar{c} \to a + b + \bar{c}$

(see Figure 11).

With the use of Regge theory, some things can be said about this cross section, at least in certain kinematic regions. We define the usual Mandelstam variables for the reaction

$a + b \to c + d$

as
$$s = (P_a + P_b)^2 = (P_d + P_c)^2$$
$$t = (P_c - P_a)^2 = (P_d - P_b)^2$$
$$u = (P_c - P_b)^2 = (P_d - P_a)^2$$

It can be shown that for both t and u large (central region), $tu \sim E_T^2 s$. This is known as the double Regge limit and schematically can be shown as in Figure 12. The Regge amplitude can be written as

$$A \sim t^{\alpha_t(0)}\, u^{\alpha_u(0)}\, f(P_T)$$

Assuming double Pomeron exchange, this reduces to

$$A \sim (tu)^{\alpha_P(0)}\, f(P_T) \sim s^{\alpha_P(0)}\, f(P_T)$$

where we have taken t, u large. Taking $\alpha_P(0) = 1$, the spectrum is then

$$E\frac{d\sigma^c}{d\vec{P}} \sim \frac{1}{s} A \sim s^{\alpha_P(0)-1} f(P_T) \sim f(P_T)$$

Assuming the leading singularities to be Regge poles,

$$E\frac{d\sigma^c}{d\vec{P}} \sim f(P_T) = \beta_a \beta_b g(P_T) = \sigma g(P_T)$$

since $\sigma = \beta_a \beta_b$.

$$\therefore \quad \frac{E}{\sigma}\frac{d\sigma^c}{d\vec{P}} = g(P_T)$$

Thus the Regge model predicts that the normalized inclusive spectrum in the central region should depend only on P_T and not on the nature of beam or projectile particle type. This is consistent with the picture drawn by the correlation length hypothesis (I-24).

In the fragmentation regions, known as the single Regge limit,

$t \to -\infty$, u fixed, $s \to \infty$ (target fragmentation)

and t fixed, $u \to \infty$, $s \to \infty$ (projectile fragmentation)
(see Figures 13, 14). Consider the target fragmentation region where

$$t \sim -\left(\frac{E_T e^{-y}}{\mu_b}\right)s$$

here $$E\frac{d\sigma^c}{d\vec{p}} = F^c(x_{11}, P_T, S) \sim \frac{t^{\alpha(0)}}{S} f(P_T, P_{11})$$

approaches $$E\frac{d\sigma^c}{d\vec{p}} \sim s^{\alpha_p(0)-1} f(P_T, P_{11}) \sim f(P_T, P_{11})$$

again assuming $\alpha_p(0) = 1$. But since

$$f(P_T, P_{11}) = \beta_a g_b(P_T, P_{11}) \text{ and } \sigma = \beta_a \beta_b, \frac{E}{\sigma}\frac{d\sigma^c}{d\vec{p}} \sim g_b(P_T, P_{11})$$

which is a spectrum independent of the projectile and of s. In a similar fashion it can be shown that in the projectile region,

$$\frac{E}{\sigma}\frac{d\sigma^c}{d\vec{p}} \sim g_a(P_T, P_{11})$$

which is independent of the target and s.

These conclusions are the same as obtained from the purely phenomenological arguments of limiting fragmentation and finite correlation length. Thus there is some self consistancy in the entire picture. Whether these pictures based on phenomenology are really representative of what happens can be answered only in the context of a dynamical theory such as hopefully QCD develops into.

The basic language reviewed in this section will be used throughout the remainder of this presentation and specialized language will be introduced, as needed.

II. THE FERMILAB HYBRID SPECTROMETER

A. Historical Note

The apparatus to be described here was built and employed in 1973 by a consortium of institutions known as the Proportional Hybrid Spectrometer Consortium[17] in conjunction with Fermilab. The experiments carried out with this system by this consortium are designated as E154 and E299, for which I. A. Pless of M. I. T. is spokesman. The basic

idea behind this system is to incorporate electronic detectors (multiwire proportional chambers) in front of and behind the 30" hydrogen bubble chamber in order to improve the detection and measuring capability of fast outgoing particles and also to be able to measure with high precision the slower particles observed in the bubble chamber. Since on the average half of the particles in an event have $x < 0$, the number of slow particles in the laboratory (bubble chamber) is substantial despite the high energies attainable at Fermilab. Perhaps this point can most easily be demonstrated by observing a "typical" event with 150 GeV/c incoming projectile momentum (see Figure 15). Note the presence of slow tracks (small radius of curvature) as well as fast tracks (nearly straight tracks). In order to obtain good momentum resolution, the curvature of these tracks have to be precisely measured.

In addition to using the electronic detectors for spatial measurements of particles, the system in the beam line before the bubble chamber is used in conjunction with Čerenkov counters to "tag" the identity of the incident particles. This is especially useful with positive beams since there are no particle separators in the beam and the amount of π^+ and P can be comparable.

B. Description of the Hybrid System

A schematic of the system as of 1976 is shown in Figure 16. Ten planes of proportial wire chambers with sensitive area 10 cm × 10 cm and wire separation of 2 mm are situated in the beam. There are 16 planes behind the bubble chamber with 30 cm × 30 cm sensitive area and 2 mm wire spacing.

A scale drawing of the bubble chamber, its magnet, and downstream detectors is shown in Figure 17. Despite the relatively small aperture of the proportional wire planes, the momentum acceptance of the system is quite good as can be seen in Figure 18. This is a consequence of the arguments given in section IA which led to relation (I-3) for small production angles.

The magnetic field distribution is shown in Figure 19. The pertinent facts to note is that the field is very uniform throughout the volume of the bubble chamber, which facilitates track reconstructions, and that the fringe field extends considerably beyond the volume of the chamber.

The integral of the field magnitude along a particle's path can be shown to be related to its momentum and turning angle by

$$\theta = \frac{0.03}{P} \int Bdl \quad \text{rad - GeV/c/Kgauss - m}$$

The average value of $\int Bdl$ from the center of the chamber is $\sim$22 Kgauss - m which allows for a turning angle of $\sim$6 m rad for a 100 GeV/c particle. The measurement of such a small turning angle in the bubble chamber is rather difficult. However, with the 6 meter lever arm of the spectrometer the determination of θ is much easier. In practice the track is measured both inside and outside the bubble chamber as depicted in Figure 20, for an hypothetical event, and the combined information is used to determine the momentum of the tracks. In this manner, the average resolution of a track with momentum P is found to be

$$\frac{\Delta P}{P} \sim 6 \times 10^{-4} \; P \; (GeV/c)^{-1}$$

To demonstrate the effectiveness of the hybrid system we show in Figure 21a the momentum distribution of 147 GeV/c beam particles as measured in the bubble chamber alone. Note how broad the distribution is due to the poor momentum resolution. When the information from the proportional wire chambers is used in conjunction with the bubble chamber for the same tracks, the resolution is markedly improved as seen in Figure 21b.

Another highly advantageous aspect of the hybrid technique stems from the fact that all charged particles in an event are measured, allowing for exclusive as well as inclusive studies. The statistics involved with inclusive studies is rather good since a single event contributes n (multiplicity) particle measurements. Most pure electronic systems are capable of one measurement per event and even then are plagued with systematic uncertainties due to limited acceptances, detection inefficiencies, etc. Although the average sensitivity of this Hybrid System is only 2 events/μb/day, the quality of the measurements is excellent and virtually free of systematic uncertainties.

III. SOME SELECTED RESULTS FROM THE HYBRID SYSTEM

Many papers have been published by the PHSC on physics results

obtained in E154 and E299, utilizing the Hybrid Spectrometer. Only a few selected topics will be discussed here, excluding the topological cross section, resonance production, diffractive dissociation and other studies. A more detailed account of what will be discussed here and on the other topics can be found in references 19-28, and those contained therein.

A. Limiting Target Fragmentation[28]

Since our experiments E154 and E299 dealt with $\pi^{\pm}$, P interactions on protons at only one momentum, 147 GeV/c ($s \sim 288$ GeV^2), we cannot test the scaling hypothesis as a function of s as discussed in section IB. However, a good test can be made of the target fragmentation hypothesis since the positive beam consisted of a mixture of protons and π^+s and thus comparing negative and positive particle production from P and π^+, we can perform systematic free comparisons. Figure 22 displays the x spectrum of positive particles produced in PP and π^+P collisions. The agreement of the spectra for $x < 0$ (target fragmentation region) is very good which is an indication of the validity of the hypothesis. A similar plot for negative produced particles is shown in Figure 23, again verifying limiting target fragmentation. Of course the forward hemisphere ($x > 0$) cannot be compared since the projectiles are diferent (π^+, P).

B. Average Multiplicity[24,25,29]

As we saw in section IC, the averaged multiplicity in the reaction

$$a + b \rightarrow X \qquad \text{(III-1)}$$

depends on $\sim$ln s, due to the following:

1) The rapidity spectrum has a flat plateau in the central region (see Figure 24).

2) As $s = (P_a + P_b)^2$ increases, the plateau extends (dashed curve) but the fragmentation regions (shaded areas) do not.

This follows from the hypothesis that the fragmentation region is limited and does not depend on s and that $\frac{dn}{dy}$ is constant in the central region. The range of the plateau was shown to be $\Delta y \sim \ln \frac{s}{\mu_a \mu_b}$ and thus it was shown that $\langle n \rangle \sim A + B + C \ln s$ (see I-27). With a change in notation, this is shown diagramatically in Figure 25. We may then state the average multiplicity as

$$\langle n \rangle = n_a(\text{Properties of a only}) + n_b(\text{Properties of b only}) + \frac{dn}{dy}(\text{const}) \ln \frac{s}{\mu_a \mu_b}$$

Within the framework of Mueller - Regge formalism, one can show[29] that for

$$a + b \rightarrow c + X \qquad \text{(III-2)}$$

a similar description evolves for fixed t_{ac} (see Figure 26) and where

$$\langle n_x \rangle = n_{E_{ac}}(t, \frac{s}{M_x^2}) + n_b(\text{Properties of b only}) + \frac{dn}{dy}(\text{const}) \ln \frac{M_x^2}{\mu^2}$$

To summarize, the average multiplicity for system X in reaction (III-1) should be

$$\langle n_x \rangle = A'' + B \ln s \qquad \text{(III-3)}$$

whereas that for reaction (III-2) should be

$$\langle n_x \rangle = A''(t, \frac{s}{M_x^2}) + B \ln M_x^2 \qquad \text{(III-4)}$$

The point is that the constant B for both reaction types, is a measure of the height of the plateau, and has the same value. Table 1 from ref. 25 is a compilation of the A" and B values for a multitude of reactions of types (III-1) and (III-2). The details of this complex analysis can be found in ref. 25 and the main point here was to illustrate the extension of the finite correlation length and limited fragmentation hypotheses in the context of Mueller - Regge formalism. As one can see from Table 1, the various B values are the same within statistical errors, for these many reactions.

The interesting result here is that in reaction (III-2) the virtual

exchange object E_{ac} can be treated as a real object whose properties depend on its virtual mass, t, and the fraction of energy available for the production of the other particles, $\frac{s}{M_x^2}$.

C. Charge Transfer - Local Compensation[20,30]

The picture of multi-hadron production as we have seen up to now seems consistent with limiting fragmentation and finite correlation length. Thus it seems natural to expect the target and projectile fragments to reconstitute the quantum numbers of their respective parents. By this we mean that the particles in the shaded areas of Figure 24 may have net charge and other internal quantum numbers (parity, strangeness, etc.) equal to those of the original particles a and b. If this in fact occurs, the implication is that the central region must then have quantum numbers representing the vaccum, i.e., net charge = 0, parity even, strangeness 0, etc. Of course if limiting fragmentation has not yet occured (s not large enough) the fragments from region a and b may overlap and we cannot expect to have a totally inert central region.

Can we expect a central plateau at 147 GeV/c? To answer this question we need to know the value of the correlation length L. Indications from experiment are that limiting fragmentation occurs at $P_{beam} \gtrsim 10$ GeV/c in P-P collisions. This implies $s \sim 21$ GeV^2 and since the region of fragmentation is $\sim L$,

$$L \sim \Delta y \sim \ln 21 = 3$$

The central plateau then begins when

$$\Delta y \sim 2L \sim 6 = \ln \frac{s}{\mu^2}$$

$$\text{or} \quad s \sim 400 \rightarrow P_{beam} \sim 200 \text{ GeV/c}$$

Theoretical arguments give $L \sim 2$ which implies that the onset of the central plateau occurs at $P_{lab} \sim 30$ GeV/c. Thus the plateau can be expected to appear at laboratory beam momenta between $\sim$30 and $\sim$200 GeV/c. This seems to be born out by the fact that Figure 27 which is a

plot of the difference of the positive and negative particle spectra, for π^- incident on protons at 147 GeV/c (E154), does not show a distinct neutral region around $y \sim 0$, implying the fact that 150 GeV/c is barely at the threshold for the existence of a central plateau. However, the positive excess ($y < 0$) and negative excess ($y > 0$) areas indicate that the original charges of target (P) and projectile (π^-) are associated with the appropriate fragmentation regions.

One way to quantitatively study the nature of the central region is to examine the charge transfered across a rapidity gap, as a function of the gap length. In doing this, it should be possible to determine the region of charge neutrality, and more interesting, is the prospect of studying whether quantum numbers such as charge are "locally compensated". By this latter statement we mean whether particles are produced in the central region in groups, or clusters, occupying somewhat small volumes of phase space in which the net quantum state is that of the vaccum, from which the particles are created.

The charge transfered across a rapidity gap Δy is defined as:

$$u(\Delta y) = \frac{1}{2}[(q_f - q_{beam}) - (q_b - q_{target})] \qquad \text{(III-5)}$$

For the case of π^- incident on protons, this reduces to

$$u(\Delta y) = \frac{1}{2}(q_f - q_b) + 1$$

q_f and q_b are the algebraic sums of the charges forward of the gap Δy and backward, respectively. Δy is symmetrically centered about $y^* = 0$. Thus if $u(\Delta y) = 0$, this implies that the net charge in the gap region Δy is 0, since the charges of the projectile and target are reconstituted by the particles in the regions forward of $\Delta y/2$ and backward of $-\Delta y/2$, respectively. If a neutral plateau exists, one should find $u(\Delta y) = 0$ (ideally) from $\Delta y = 0$ to $\Delta y = L_p$ where L_p is the length of the plateau. Of course in practice we would expect $u(\Delta y)$ to fluctuate. The behavior of the fluctuation is interesting in itself, especially for Δy centered about $y^* = 0$, because it can be a measure of whether particles are formed in groups or "clusters" with fixed internal energies and internal quantum numbers[30,31]. The fluctuation in charge transfer can be measured by the dispersion function

$$D^2(\Delta y) = \langle u(\Delta y)^2 \rangle - \langle u(\Delta y) \rangle^2 \qquad \text{(III-6)}$$

where the averaging is done over events.

Let us assume particles to be formed in groups or clusters having non-zero internal energy. Assume further that because of this internal energy, the particles are able to travel in rapidity space a distance $\pm \Delta y_0/2$ from their energy centroid when the clusters "decay". If the clusters are produced randomly throughout the central region, as implied by the presence of a plateau, on the average, only those clusters situated within $\pm \Delta y_0/2$ from $y^* = 0$ would be able to transfer net charge from one hemisphere to the other. The fluctuation in the charge transfer, $D^2(\Delta y)$, is then expected to be a maximum for $\Delta y = 0$ and slowly decrease as Δy increases, until $\Delta y = \Delta y_0$. However, for $\Delta y > \Delta y_0$, as much charge is transfered into the gap as transfered out of the gap, resulting in a constant value of D^2 (we assume the density of clusters to be uniform). The fact that the clusters may themselves be moving does not change these conclusions provided their motion is random. Thus the width of the fall-off in D^2 is a measure of the "size" or more accurately, the internal energy, of the clusters. An hypothetical $D^2(\Delta y)$ distribution depicting this situation is shown in Figure 28. For this case, $\Delta y_0 \sim 1.5$. If we assume the clusters to decay into 2π mesons, then

$$\Delta y_0 \sim \ln \frac{s_{\pi\pi}}{2\mu_\pi} \sim 1.5$$

and the energy available for kinetic energy of the two pions is

$$Q = \sqrt{s} - 2\mu_\pi = \mu(e^{.75} - 2) \sim 16 \text{ MeV} .$$

The internal energy would correspond to $\sim$300 MeV.

In Figure 29 we display $D^2(\Delta y)$ distributions from E154[20] for various topologies, and from these curves we can infer the drop off in D^2 to be $\sim$1-2 units wide. Thus we conclude that clusters of $\sim$1-2 units are perhaps being formed in this reaction. The drop off to $D^2 \sim 0$ after the relatively constant region is due to kinematic limitations and thus is of no consequence here.

The transverse momenta of particles produced could also be considered

an internal quantum number and its local compensation is expected if clusters are formed. In order to study this, consider the quantity

$$C(\Delta y) \equiv - \langle \vec{P}_{T,f} \cdot \vec{P}_{T,b} \rangle \qquad \text{(III-7)}$$

which is the average over events of the scalar product between the net transverse momentum vector ($\vec{P}_{T,f}$) forward of the Δy gap and the net transverse momentum vector ($\vec{P}_{T,b}$) backward of the gap. As Δy is increased from 0, the contributions of the correlated $\vec{P}_T$ of the cluster decay particles in the forward and backward hemisphere, which are most substantial for $\Delta y = 0$, should drop off as Δy approaches the "size" of the cluster. Beyond this point, the net transverse momenta vector becomes steadily random in both direction and magnitude resulting in a steady decrease of $C(\Delta y)$. This effect is easily seen in Figure 30, again supporting the conclusion that clusters of "size" about 1-2 rapidity units are perhaps being formed.

Thus it seems that in spite of the fact that we do not observe a definite rapidity plateau at 147 GeV/c, we are at the threshold of its formation and the possible formation of clusters is evident. The picture seems consistent with randomly formed clusters, having internal energies of a few hundred MeV.

D. The Leading Charge Model[26,27]

As we saw in the previous section, charge seems to be locally compensated in the central region despite the absence of a definite neutral region. Here we attempt to isolate the central region on an event to event basis by use of the zone graph[32] and then look into the properties of the central region.

Figure 31 is a schematic of an ideal 10 particle event displaying the charges of the particles along with their rapidity values. The zone graph Z(y) is then constructed according to

$$Z(y) = \sum_{i=1}^{N} q_i \theta(y-y_i) - q_b \theta(y-y_b) - q_t \theta(y-y_t) \qquad \text{(III-8)}$$

where q_i = charge of i^{th} particle

$$\theta(y-y_i) = 1 \qquad y \geq y_i$$
$$= 0 \qquad y < y_i$$

The idea is to form a zone graph for each event and exclude the particles in the beam and target zones (shaded areas in Figure 31). The particles in the remaining central zones are then defined to be from the central region. The question we now ask is, are these particles in the central region randomly produced and governed by thermodynamics, as in a "fireball" model[33-35]? To study this question, self-consistent checks are made on the data, based on three models:

1) RCM (Random Charge Model)
   The charges of the particles are randomly re-assigned in each event, keeping the originally measured 4-vectors.
2) ECM (Extreme Charge Model)
   The charges in an event are systematically re-assigned in a +, -, +, -, +, - - - alternating sequence starting from the target and ending with the projectile.
3) LCM (Leading Charge Model)
   The charge assignments in the beam and target zones are not altered but those of the central region are randomly reassigned.

These reassignments of charges for the three models are schematically shown in Figure 32 for the same hypothetical event of Figure 31.

Artificial data sets are then created for each of these models, all utilizing the actually measured 4-vectors, and various analyses are carried out on these artificial data sets and compared with the corresponding analyses carried out on the real data set. The rational for this procedure is that the correct model should reproduce all aspects of the data. Figures 33-35 show the results of these comparisons for charge transfer, probability for zone population, and zone distributions, respectively. In all cases the LCM seems to duplicate the true data sample. This implies that the central region, as defined by the zone graph method, is indeed random as far as charge distribution is concerned (the local compensation of charge is compatible with this statement). A further indication of this can be seen in Figure 36 where the asymmetry in charge distribution

$$A(y) = \frac{\frac{d\sigma^+}{dy} - \frac{d\sigma^-}{dy}}{\frac{d\sigma^+}{dy} + \frac{d\sigma^-}{dy}} \qquad \text{(III-9)}$$

is displayed. In the interaction C. M. S. the distribution does not have a neutral region (Figure 36a), as was already indicated in Section III^C (Figure 27). However, if one transforms the particles to the rest frame of the central region on an event ot event basis, a clear neutral region spanning about 2 units of rapidity becomes evident (Figure 36b).

We call the rest system of the central region particles the "fireball" system. If it truly is a fireball, the particles in it should display isotropic distributions of their momentum directions. Figure 37a shows the distribution of the transverse (P_T) and longitudinal (P_{11}) components of momenta in the interaction C. M. S. whereas Figure 37b shows the same distributions in the fireball system. Note how much more similar the distributions are in the fireball system than in the interaction C. M. S. The deviation from isotropy at the higher momentum values $|P| \gtrsim 500$ MeV/c is probably due to the fact that since neutral particles are not detected, the transformation to the fireball system is only approximate. The angular distribution in the fireball system is shown in Figure 38 for various momentum values. The distributions for particles with momenta less than 400 MeV/c are highly isotropic whereas above this value discrepancy from isotropy is evident. Again this is probably due to the approximate nature of the transformation to the fireball system.

As a final check on the fireball nature of the central region particles, we fit the momentum distribution to a Bose distribution

$$F(p) = \frac{AP^2}{e^{(P^2+\mu^2)^{1/2}/T} - 1} \qquad \text{(III-10)}$$

for $P < 800$ MeV/c and obtain a value for the temperature T of 131 ± 2 MeV, which is compatible with the thermodynamic picture. The experimental and fitted distributions are shown in Figure 39.

In closing, I would like to mention that research with the Fermilab Hybrid System is continuing with the next experiments utilizing larger particle detectors and a charged particle identifier, CRISIS[36,37], along with a forward gamma-ray detector, FGD[38]. This will enable us

to determine the nature of the particles produced in the central region and to study strangeness compensation, baryon number compensation, etc. Also of interest in our future experiments (E565, E570) is the insertion of nuclear targets in the bubble chamber, in the form of thin foils, which will enable the study of space-time development in hadronic interactions[39]. These new features added to the hybrid system makes this facility a unique one and the yield of new information in hadronic interactions would hopefully be considerable. The experiments will involve 4-8 times more events than any previous Fermilab hybrid experiment which will allow for good statistics and possibly the capability to embark on systematic error free studies of "jet" formations[40]. This will then open the doors to sdudies on quark recombination and hadron formation in the context of Field and Feynman[41-43] and others. Thus the path to direct QCD tests in the hybrid system may not be too far off.

References

1. J. Whitmore, Physics Reports 10C, 273 (1974)
2. J. Whitmore, Physics Reports 27C, 187 (1976)
3. Proceedings of the Conference on High Energy Particle Collisions, Vanderbuilt U., (1973)
4. W. Frazer et al., Rev. Mod. Phys. 44, 284 (1972)
5. C. E. De Tar, Phys. Rev. D3, 128 (1971)
6. D. Horn and F. Zachariasen, "Hadron Physics at Very High Energies", Frontiers in Physics Series, W. A. Benjamin, Inc. Reaing, Ma. (1973)
7. M. L. Perl, "High Energy Hadron Physics", John Wiley & Sons, N. Y. (1974)
8. L. Van Hove, Nuc. Phys. B9, 331 (1969)
9. J. E. Brau et al., Phys. Rev. Lett. 27, 1481 (1971)
10. K. G. Wilson, Acta. Phys. Austr. 17, 37 (1963)
11. K. G. Wilson, Cornell Preprint CLNS-31 (1970)
12. R. P. Feynman, Proc. of the Third Int. Conf. on High Energy Collisions, Stony Brook, N. Y. 237 (1969)
13. R. P. Feynman, Phys. Rev. Lett., 23, 1415 (1969)
14. J. Benecke et al., Phys. Rev. 188, 2159 (1969)
15. A. H. Mueller, Phys. Rev. D2, 2963 (1970)
16. A. H. Mueller, Phys. Rev. D4, 150 (1971)
17. The PHSC consists of members from the following institutions: Brown U., CERN, Fermilab, Illinois Institute of Technology, U. of Illinois, Indiana U., Johns Hopkins U., Massachusetts Institute of Technology, Oak Ridge National Laboratory, Rutgers U., Stevens Institute of Technology, U. of Tennessee, Yale U.
18. D. G. Fong et al., Phys. Lett. B53, 290 (1974)
19. D. Fong et al., Phys. Lett. B60, 124 (1975)
20. D. Fong et al., Phys. Lett. B61, 99 (1976)
21. D. Fong et al., Nuc. Phys. B102, 386 (1976)
22. D. Fong et al., Nuc. Phys. B104, 32 (1976)
23. D. Fong et al., Nuovo Cimento A34, 659 (1976)
24. PHSC, Phys. Rev. Lett. 37, 736 (1976)
25. D. Brick et al., Phys. Rev. D19, 743 (1979)
26. D. Brick et al., Nuc. Phys. B152, 45 (1979)
27. J. E. Brau, Ph.D. Thesis, MIT (unpub.) (1978)

28. A. Napier, Ph.D. Thesis, MIT (unpub.) (1979)
29. C. E. De Tar, Phys. Rev. D17, 870 (1978)
30. C. Quigg, Phys. Rev. D12, 834 (1975)
31. T. Ludlam et al., Phys. Lett. B48, 449 (1974)
32. A. Krzywicki and D. Weingarten, Phys. Lett. B50, 265 (1974)
33. M. Miesowicz, Progress in Elementary Particle and Cosmic Ray Physics 10, 103 (1971)
34. I. M. Dremin and A. M. Dunaevskii, Phys. Reports 18, 159 (1975)
35. R. Hagedorn, Nuovo Cim. Supp. 3, 147 (1965); 6, 311 (1968)

35a. R. Hagedorn and J. Ranft, Nuovo Cim. Supp. 6, 169 (1968)

36. V. Kistiakowsky, "Particle Identifiers for Hadron Physics", NALREP, 13 (July, 1976)
37. B. F. Wadsworth et al., IEEE Trans. on Nuc. Science, NS26, 120 (1979)
38. M. Heller et al., Nuc. Instr. and Methods 152, 379 (1978)
39. W. Busza, Proc. of the VIIth International Colloquium on Multi-particle Reactions, Tutzing, (June 1976)
40. I. A. Pless, IXth International Symposium on High Energy Multiparticle Dynamics, Tabor, Czechoslovakia, (1978)
41. R. D. Field and R. P Feynman, Phys. Rev. D15, 2590 (1977)
42. R. D. Field and R. P. Feynman, Nuc. Phys. B136, 1 (1978)
43. R. P. Feynman, R. D. Field and G. C. Fox, Nuc. Phys. B128, 1 (1977)

Figure Captions

1. A schematic t channel diagram depicting projectile and target fragmentation.

2. P_T spectra for $PP \to \pi^- + X$, $K^- + X$, $\bar{P} + X$ for various fixed x values and for $\sqrt{s}$ = 23, 31, 45, 53, 6.8 (from ref. 3).

3. More of the same as in fig. 1 but down to $x \sim 0.08$ (from ref. 3).

4. x spectra for $PP \to K^+ + X$, $K^- + X$ for various P_T values and for $\sqrt{s}$ = 23, 31, 45, 53, 6.8 (from ref. 3).

5. x spectra for $PP \to P + X$ for various P_T values and $\sqrt{s}$ = 23, 31, 45, 53, 6.8 GeV (from ref. 3).

6. x spectra for $PP \to P + X$ for various P_T values and s = 551, 930, 1995 GeV^2 (from ref. 3).

7. x spectra for $\pi^-P \to \pi^- + X$ and $\pi^+P \to \pi^+ + X$ for π^- beam momenta of 16, 40 and 100 GeV/c and π^+ beam momenta of 8, 16 and 100 GeV/c (from ref. 2).

8. A schematic of what a y spectrum may look like in general (solid line) and with a central plateau (dashed line).

9. Experimental y spectra for various P_T and $\sqrt{s}$ = 23, 31, 45, 53, 6.8 for $PP \to \pi^+ + X$, $\pi^- + X$, $K^+ + X$, $K^- + X$, $P + X$, $\bar{P} + X$ (from ref.3).

10. Schematic for cross section calculation for $a + b \to X$ according to the optical theorem.

11. Schematic for inclusive cross section calculation for $a + b \to c + X$ according to the generalized optical theorem.

12. Double Regge diagram for $a + b \to c + X$.

13. Single Regge diagram for $a + b \to c + X$ in the target region.

14. Single Regge diagram for $a + b \to c + x$ in the projectile region.

15. A typical hadronic interaction as seen in a bubble chamber at beam momentum of 150 GeV/c.

16. A schematic of the Fermilab Hybrid Spectrometer.

17. Scale drawing of the Fermilab Hybrid Spectrometer magnet and downstream detectors.

18. Momentum acceptances for the D, E; D, E, F; D, E, F, G chambers.

19. Magnetic field profile for the 30" bubble chamber of the hybrid system.

20. Illustration of measurement points used in an interaction for track reconstruction.

21. Beam momentum distributions.
    a) Using measured data from bubble chamber alone.
    b) Using measured data from bubble chamber and proportional wire chambers.

22. x spectra for $PP \to (+) + X$ and $\pi^+P \to (+) + X$ from the hybrid system at beam energy of 147 GeV/c (from ref. 28)

23. x spectra for $PP \to (-) + X$ and $\pi^+P \to (-) + X$ from the hybrid system at beam energy of 147 GeV/c (from ref. 28)

24. Schematic depicting the growth of the plateau, with energy, and constant fragmentation regions (shaded areas)

25. Schematic for the various regions in which particles are produced in the reaction $a + b \to X$.

26. Schematic for the various regions in which particles are produced in the reaction $a + b \to c + X$, for fixed t_{ac}.

27. Distribution of the difference in the (+) particle spectrum and (-) particle spectrum

$$\Delta\frac{d\sigma}{dy} = \frac{d\sigma^+}{dy} - \frac{d\sigma^-}{dy}$$

from E154 (π^-P at 147 GeV/c) from ref. 20.

28. An idealized $D^2(\Delta y)$ distribution expected from formation of clusters of "size" $\sim$1.5.

29. $D^2(\Delta y)$ distributions from E154 (π^-P at 147 GeV/c) taken from ref. 20.

30. $C(\Delta y)$ (see text) from E154 taken from ref. 20.

31. Schematic depicting the construction of a zone graph taken from ref. 26, 27.

32. Illustration of charge reassignments in the RCM ECM and LCM models (see text).

33. Comparison of charge transfer distributions between RCM LCM and the data (x points). ECM can only give charge transfer of 0 and therefore is not shown. (from ref. 26, 27).

34. Zone multiplicity distributions for RCM, ECM, LCM and data (x points) from ref. 26, 27.

35. Semi-inclusive zone distribution comparisons between RCM, LCM and data (x points) for various topologies (from ref. 26, 27).

36. The charge asymmetry distributions

$$A(y) = \left(\frac{d\sigma^+}{dy} - \frac{d\sigma^-}{dy}\right) / \left(\frac{d\sigma^+}{dy} + \frac{d\sigma^-}{dy}\right)$$

for a) the interaction C. M. S. and b) the central fireball system.

37. Inclusive transverse and longitudinal momenta distributions in the a) interaction C. M. S. and b) fireball system.

38. Inclusive angular distributions in the fireball system for various momentum regions.

39. Bose distribution fitted to the experimental momentum distribution.

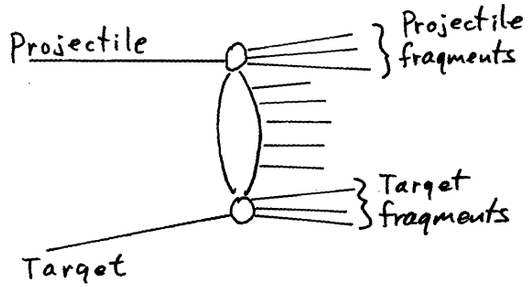
Projectile
Projectile fragments
Target fragments
Target

FIGURE 1

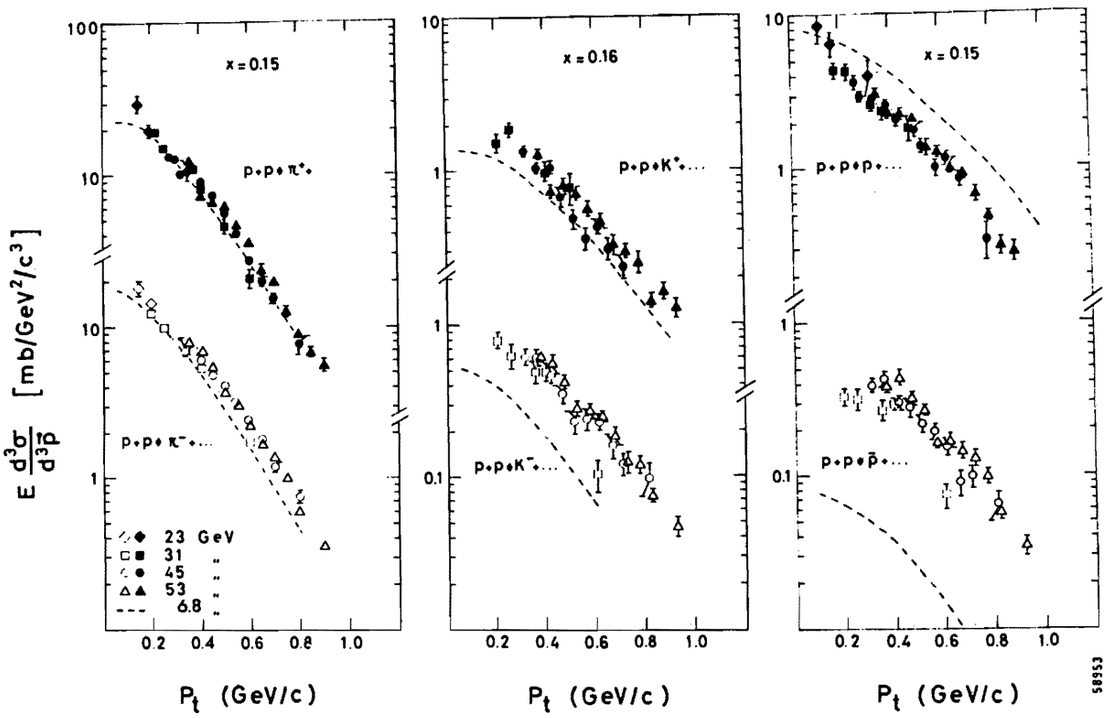

The invariant cross-section plotted versus transverse momentum P_t, at a value x = 0.15, for $\pi^{\pm}$, $K^{\pm}$, p, and $\bar{p}$.

FIGURE 2

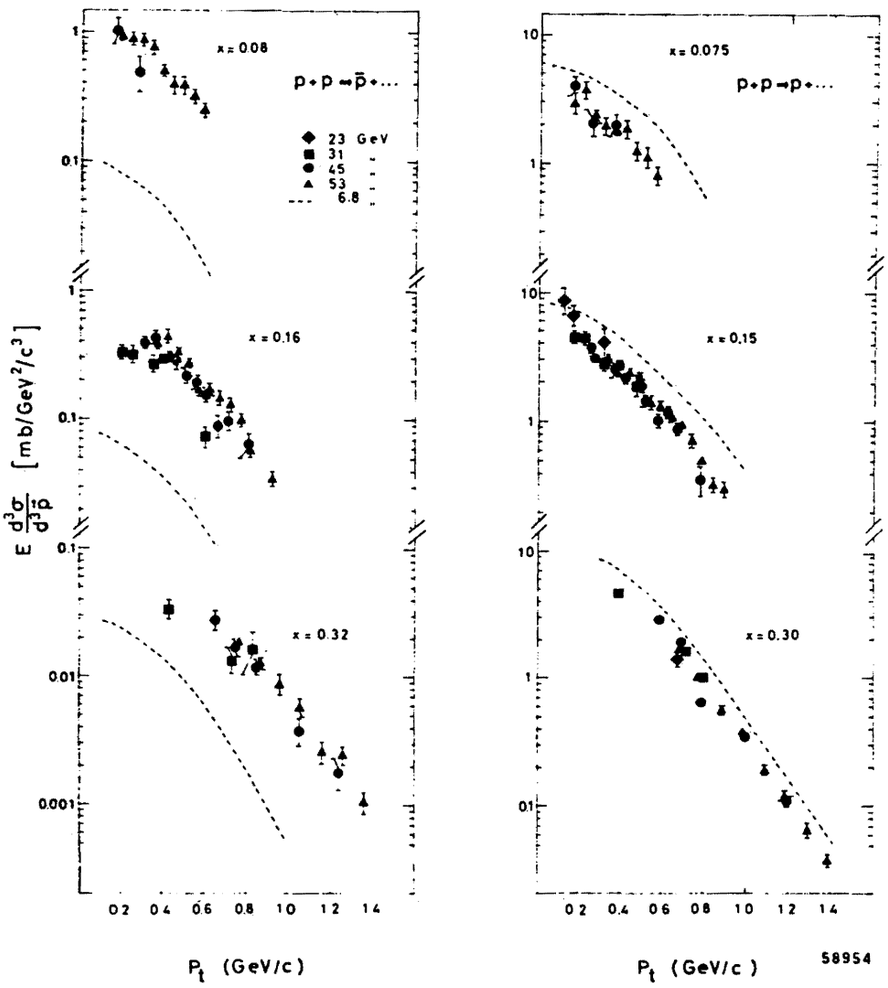

The invariant cross-section plotted versus transverse momentum P_t, at the value x = 0.075, x = 0.15, and x = 0.30, for p and $\bar{p}$.

FIGURE 3

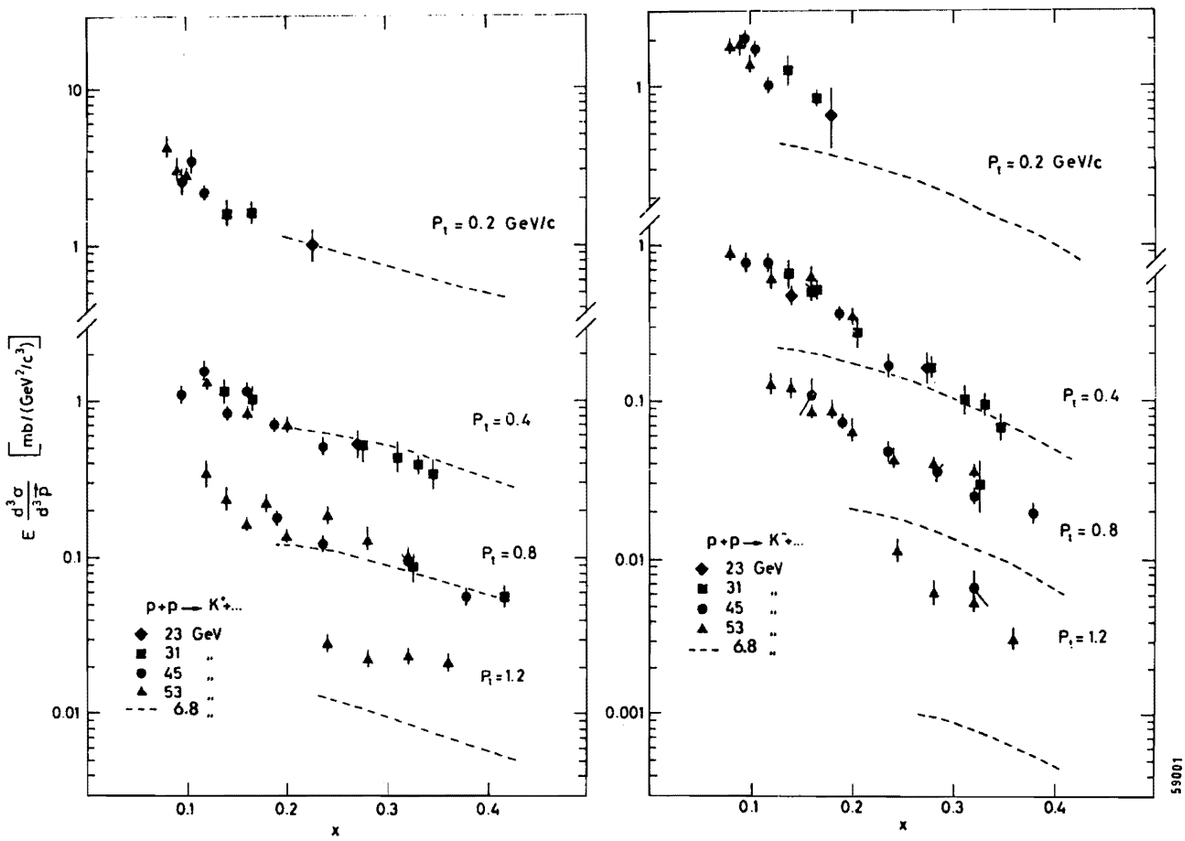

The invariant cross-sections plotted versus x, at P_t = 0.2, 0.4, 0.8, and 1.2 GeV/c, for K^+ and K^-.

FIGURE 4

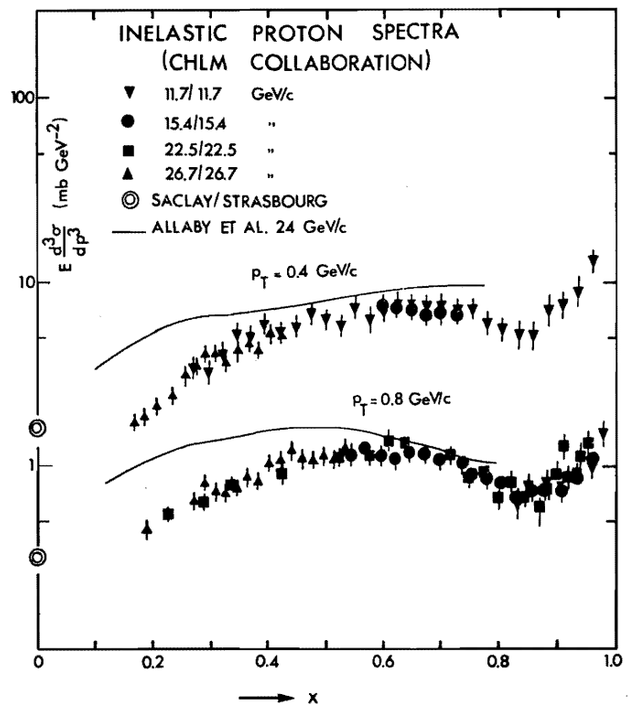

Proton spectra at fixed p_T vs. x for several energies.

FIGURE 5

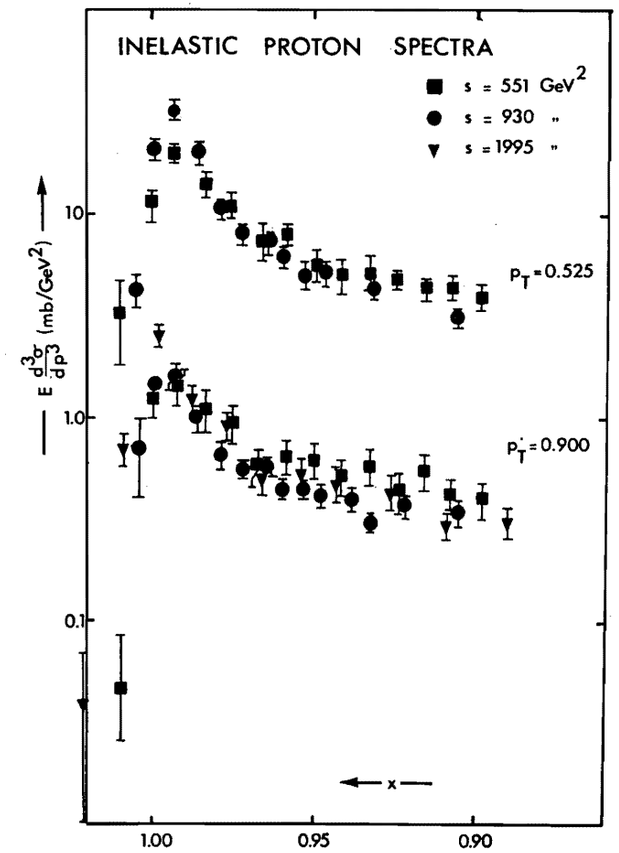

Inelastic proton spectra at fixed p_T vs. x for several energies.

FIGURE 6

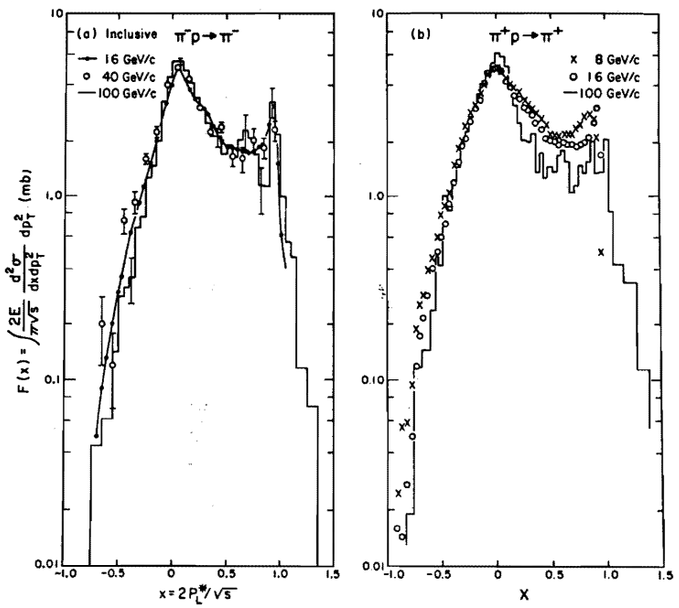

x distribution for the inclusive reactions (a) $\pi^- p \to \pi^-$ + anything, and (b) $\pi^+ p \to \pi^+$ + anything.

FIGURE 7

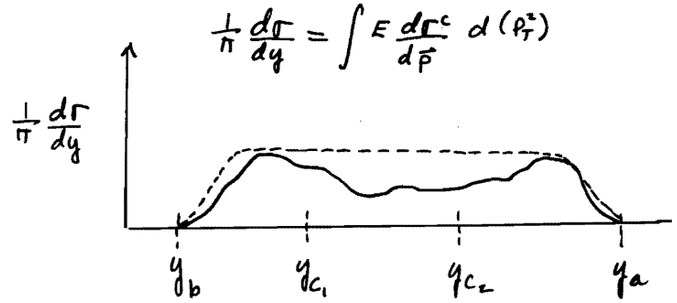

FIGURE 8

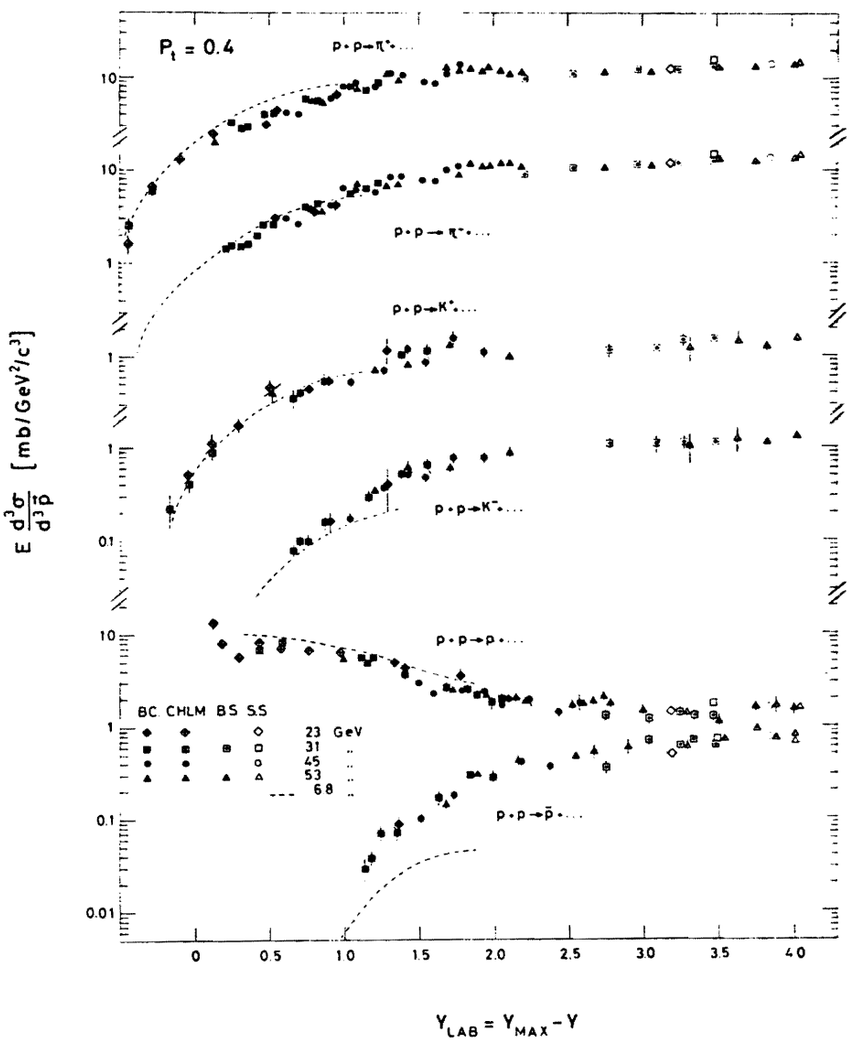

Compilation of data on the rapidity distributions, in the beam proton rest frame, of pions, kaons, protons, and anti-protons for a fixed transverse momentum p_T of 0.4 GeV/c.

FIGURE 9

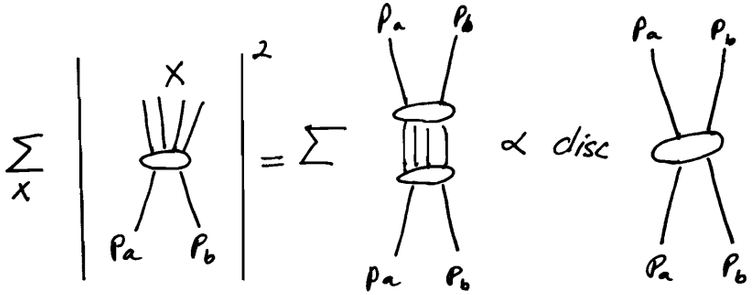

FIGURE 10

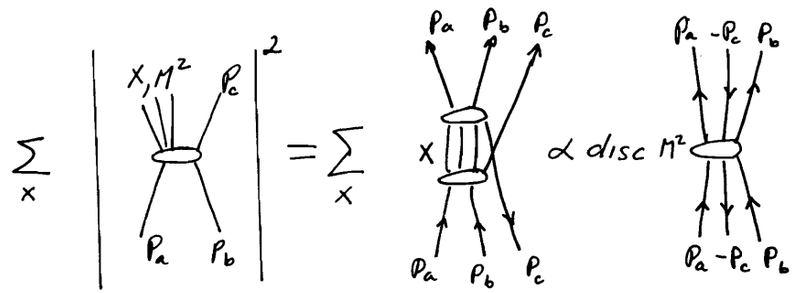

FIGURE 11

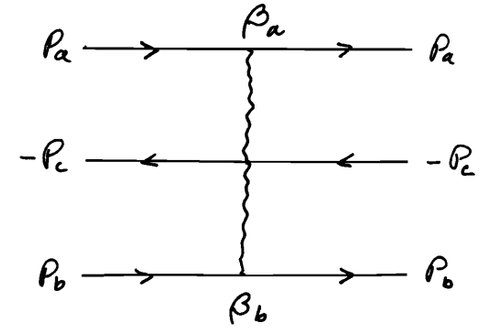

FIGURE 12

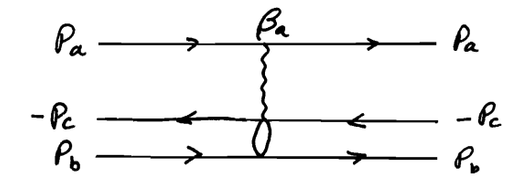

$t \to -\infty$, u fixed, $s \to \infty$
target fragmentation

FIGURE 13

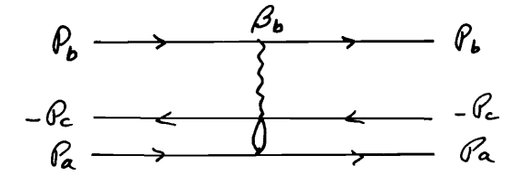

t fixed, $u \to \infty$, $s \to \infty$
projectile fragmentation

FIGURE 14

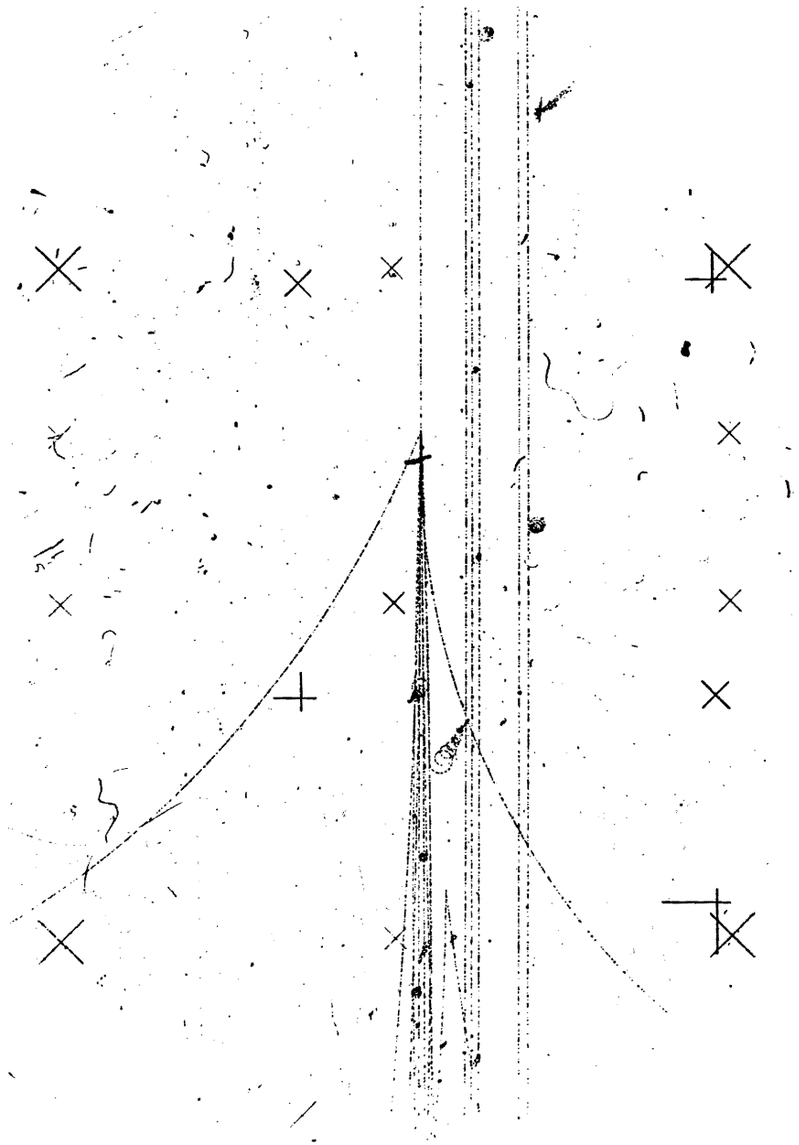

FIGURE 15

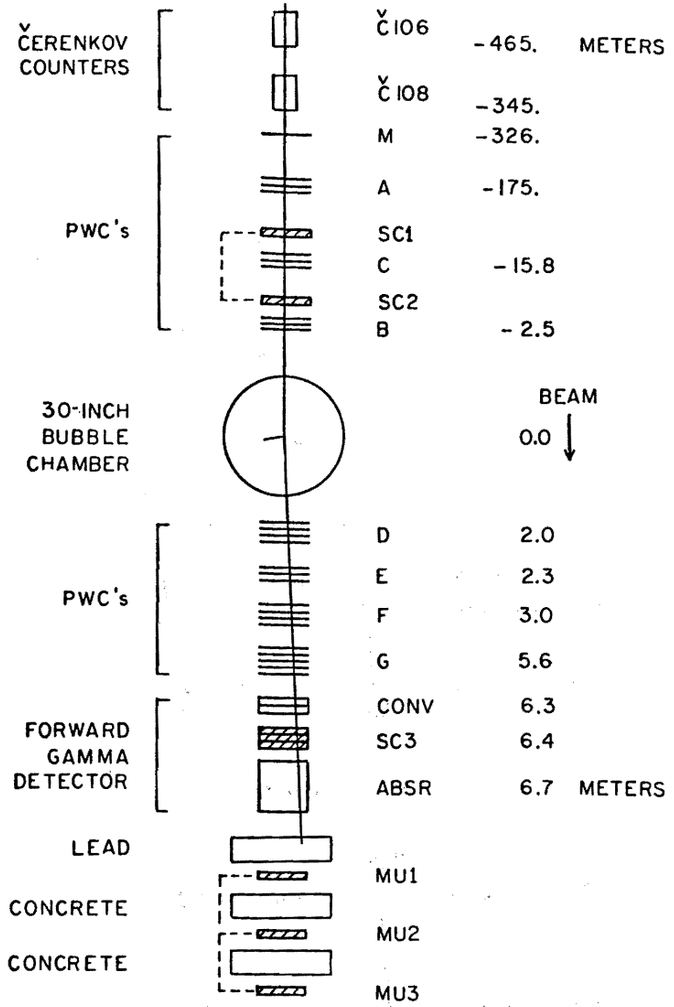

FERMILAB HYBRID SYSTEM CONFIGURATION

FIGURE 16

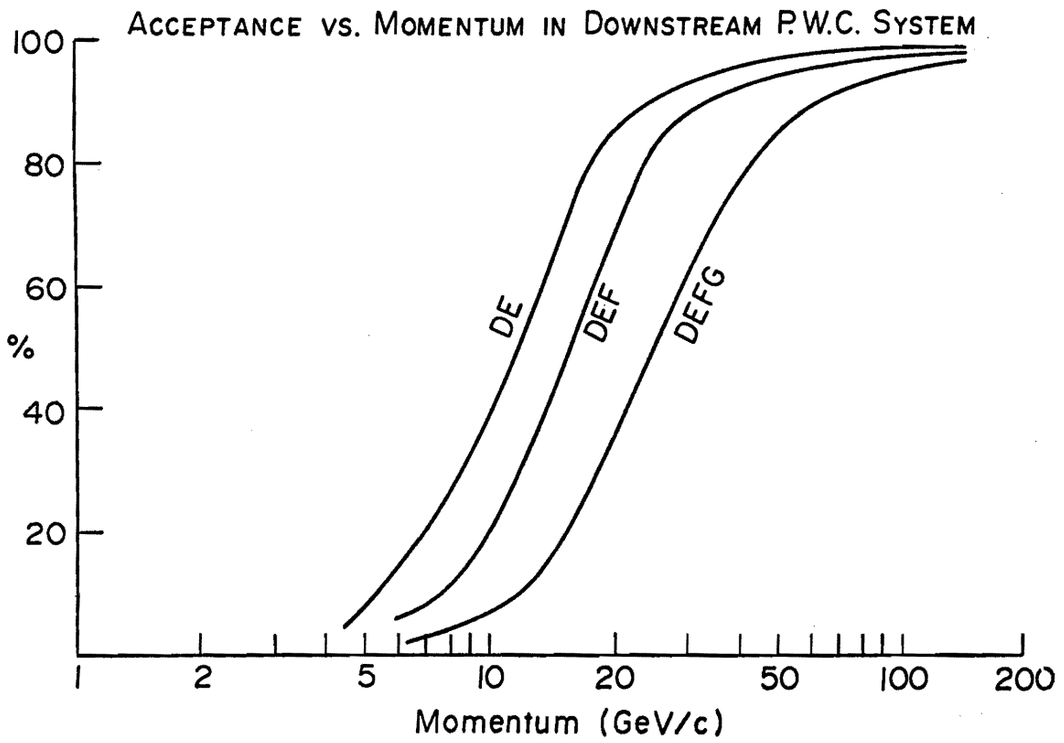

FIGURE 18

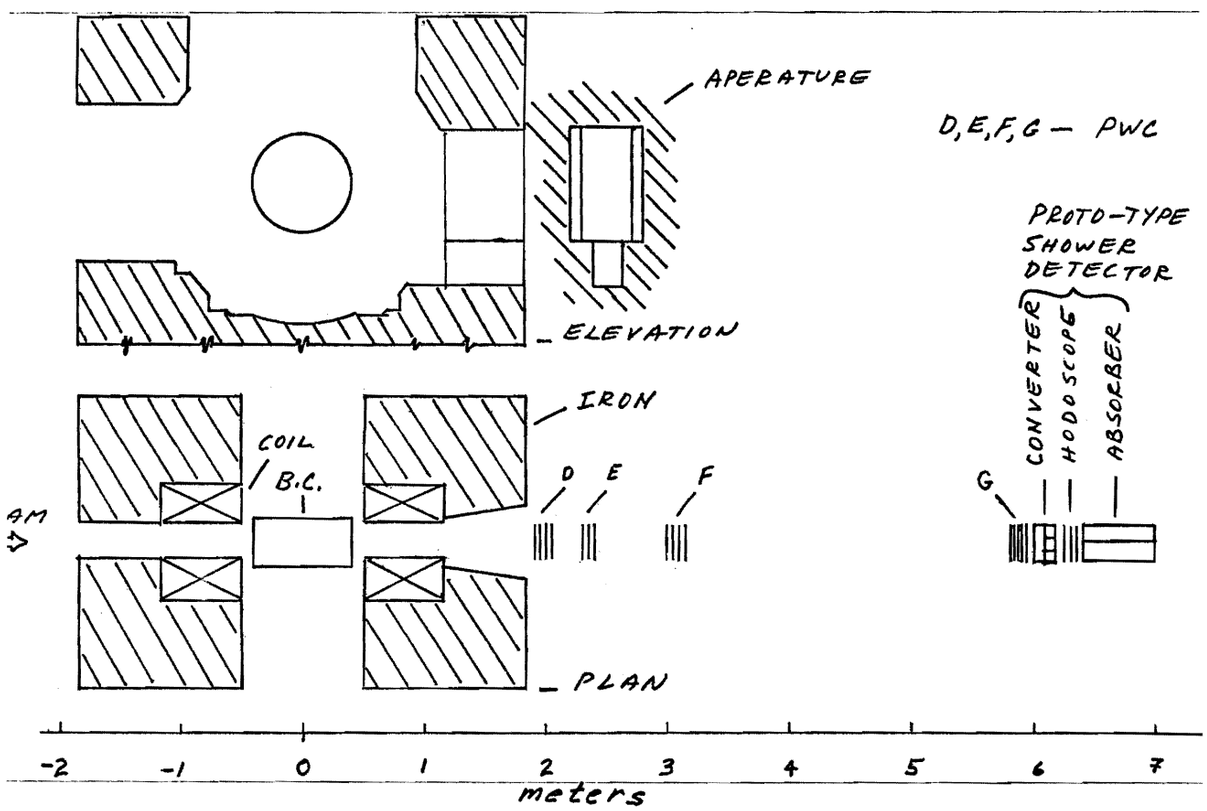

FIGURE 17

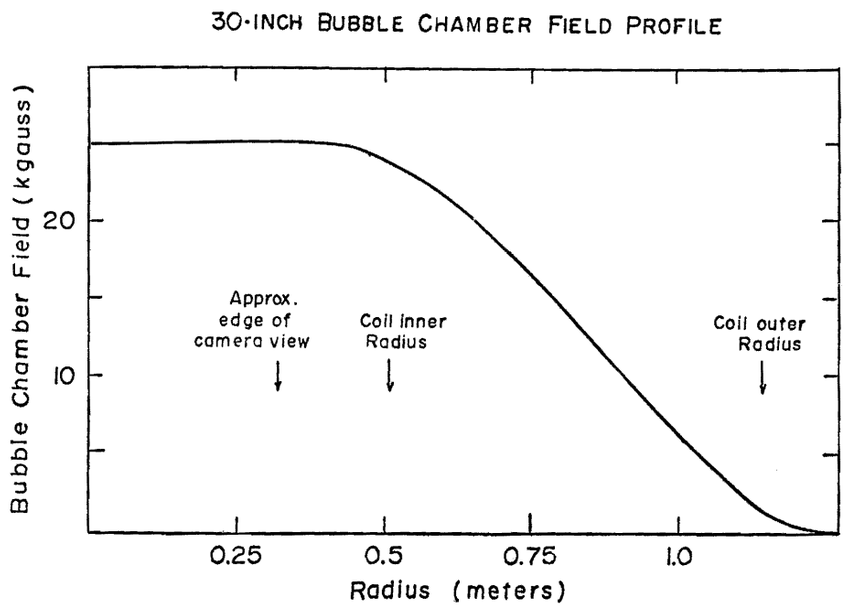

FIGURE 19

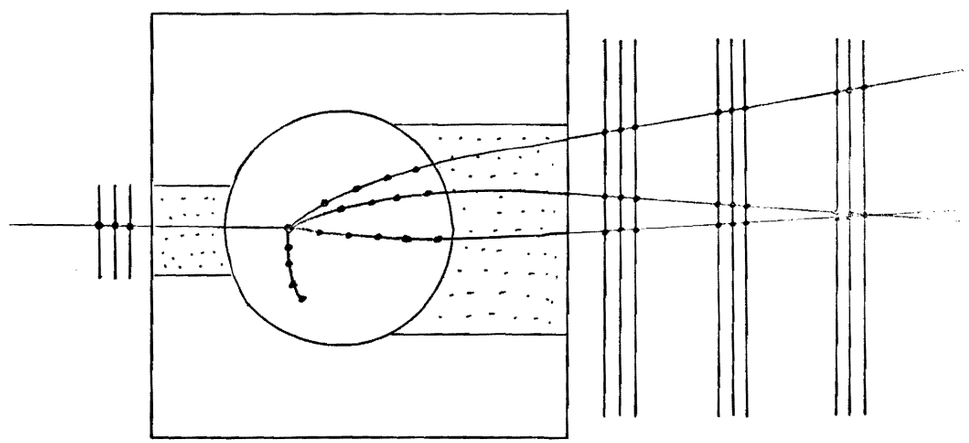

FIGURE 20

BEAM TRACK MOMENTUM DISTRIBUTIONS

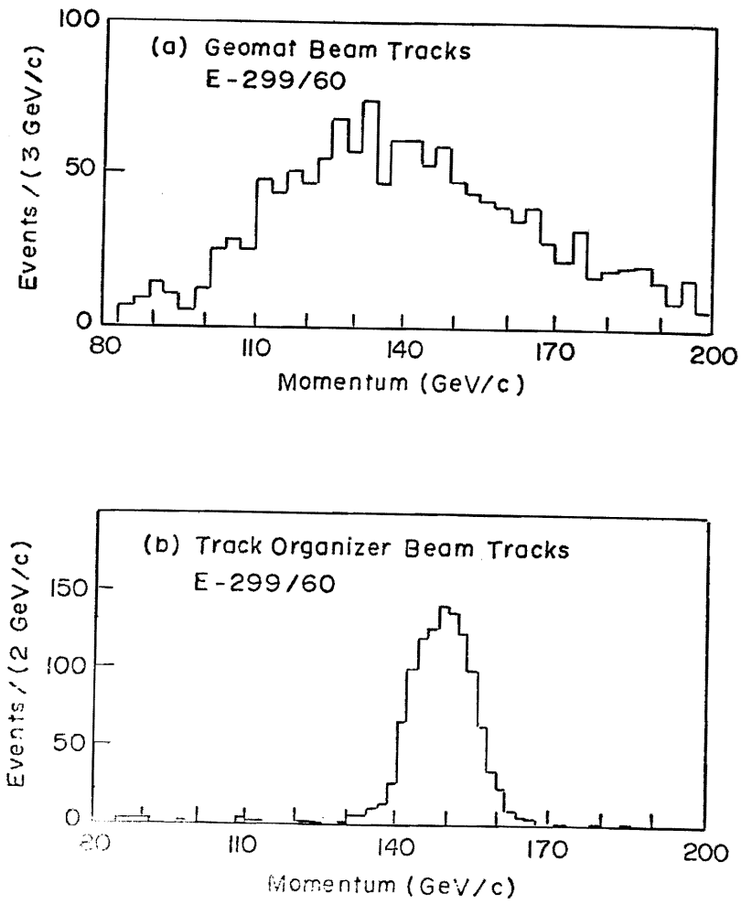

FIGURE 21

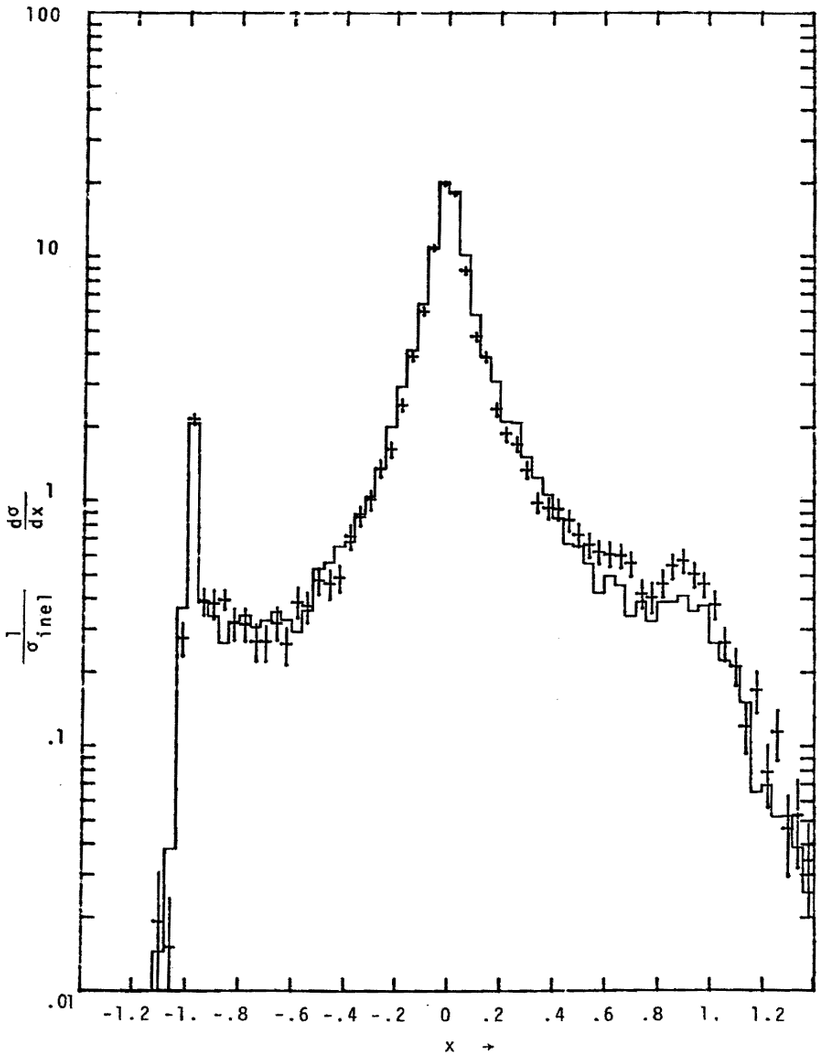

Comparison of positives from pp and $\pi^+ p$ events.

FIGURE 22

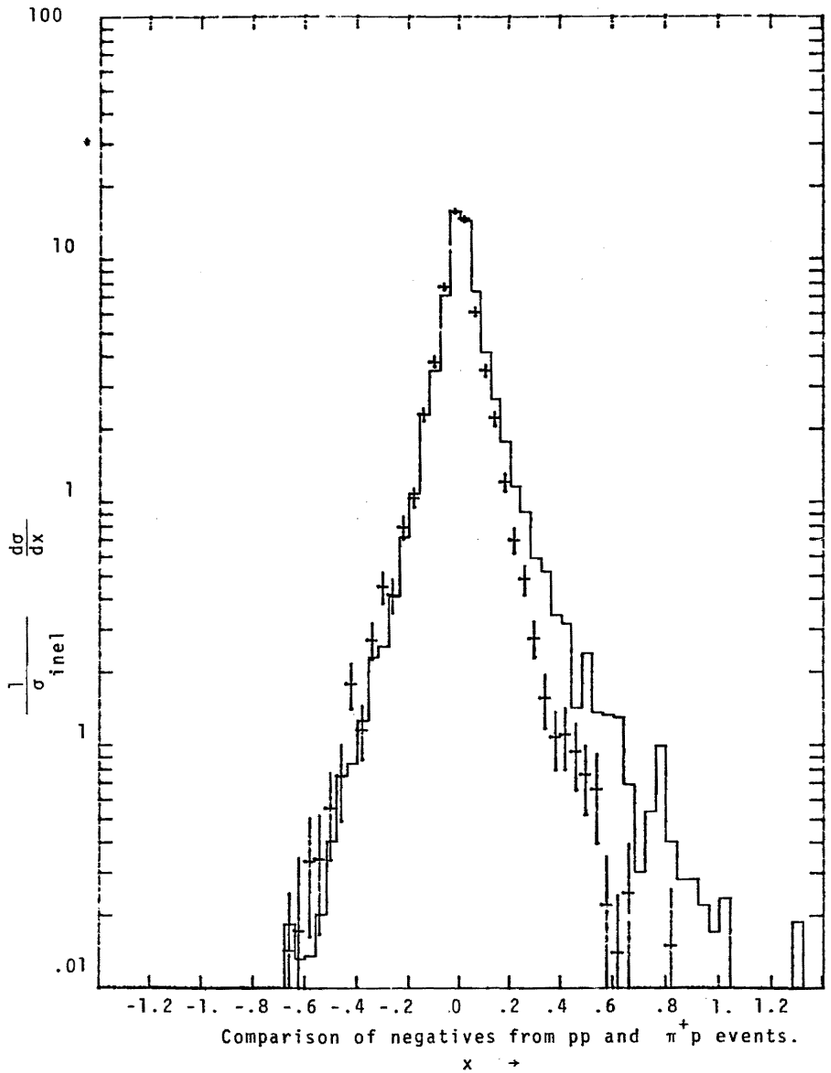

FIGURE 23

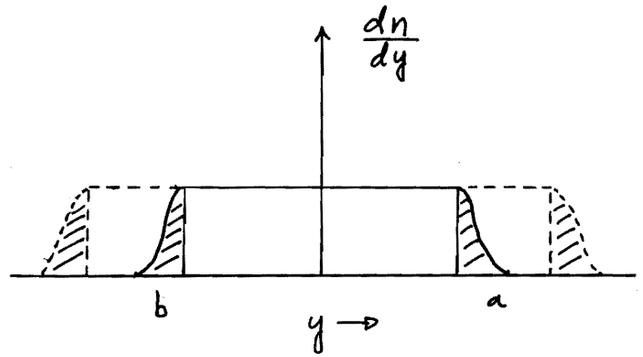

FIGURE 24

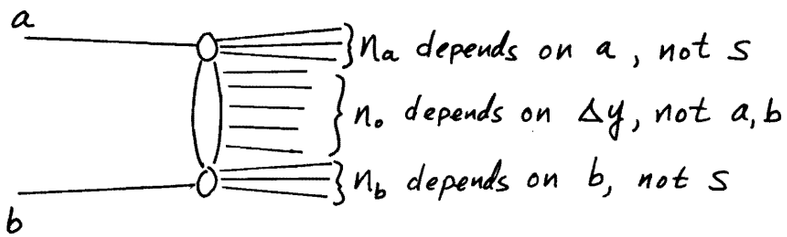

FIGURE 25

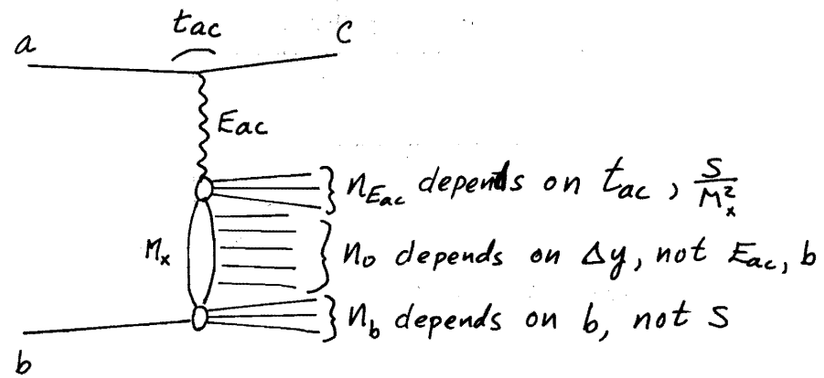

FIGURE 26

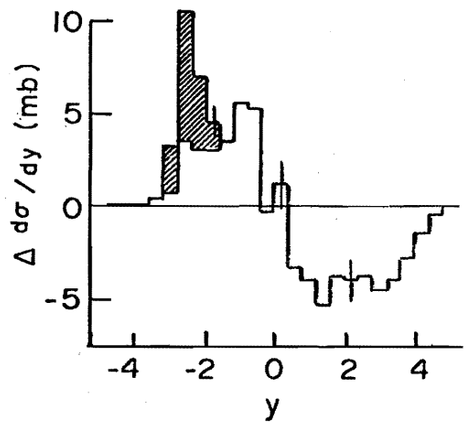

FIGURE 27

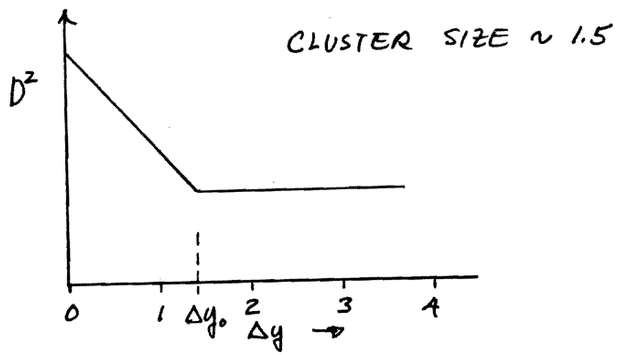

FIGURE 28

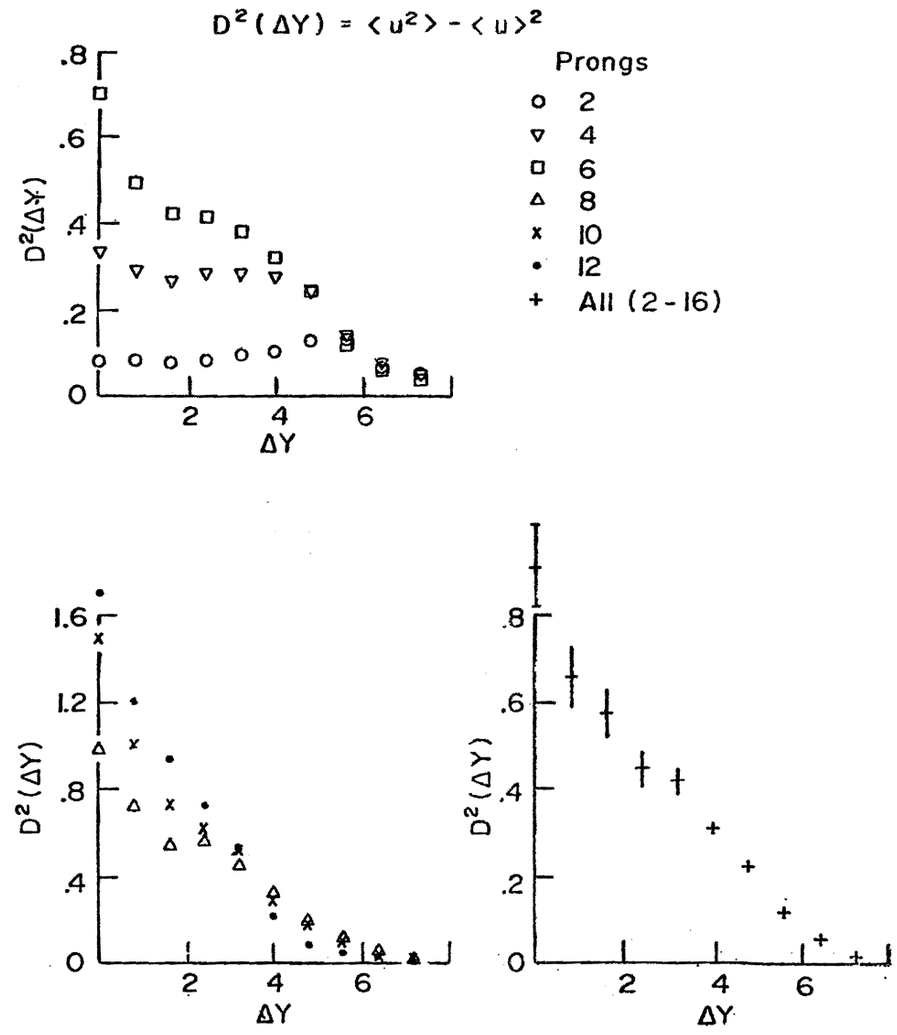

FIGURE 29

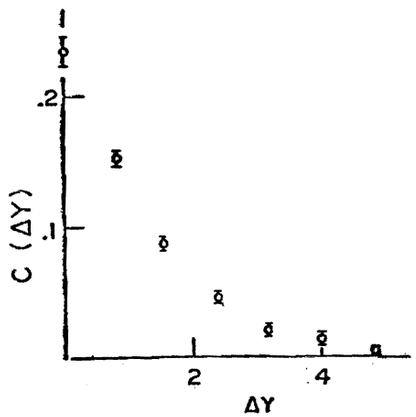

FIGURE 30

CONSTRUCTION OF A ZONE GRAPH

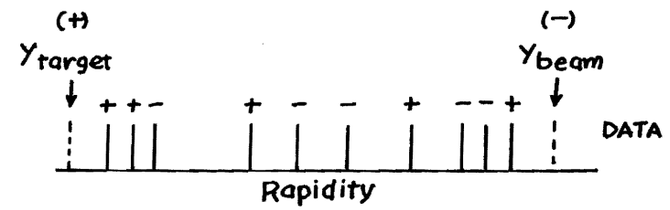

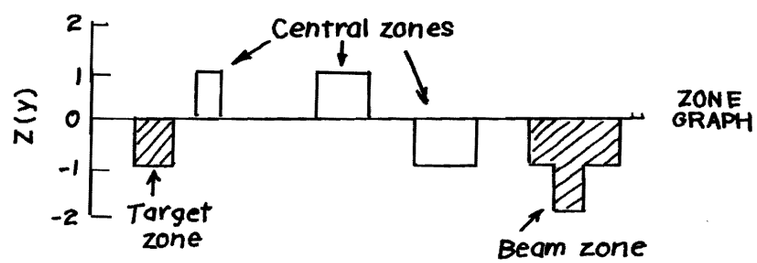

FIGURE 31

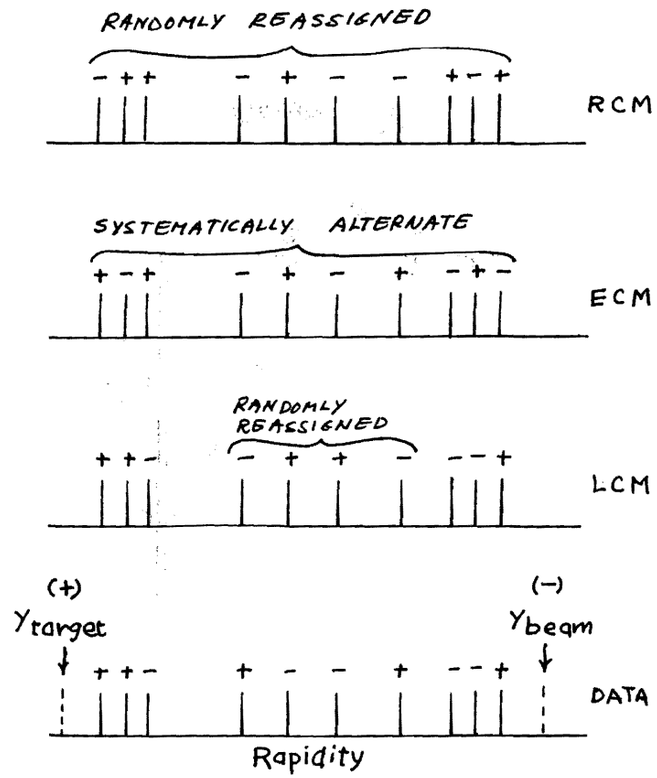

FIGURE 32

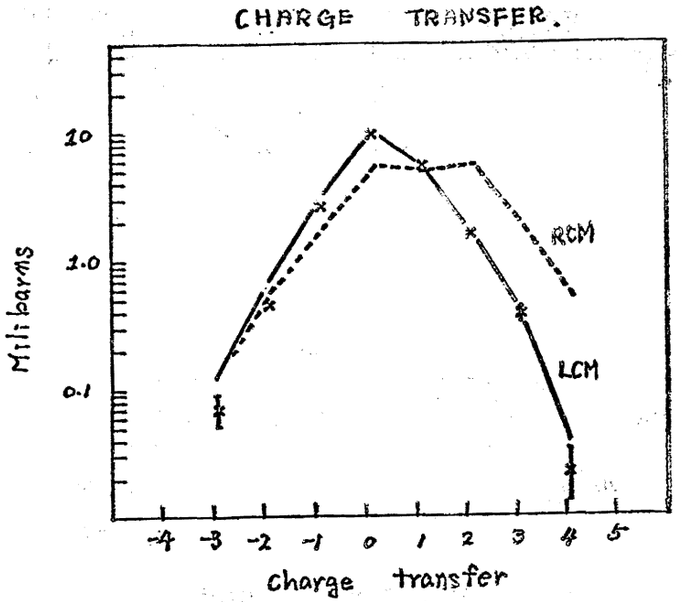

FIGURE 33

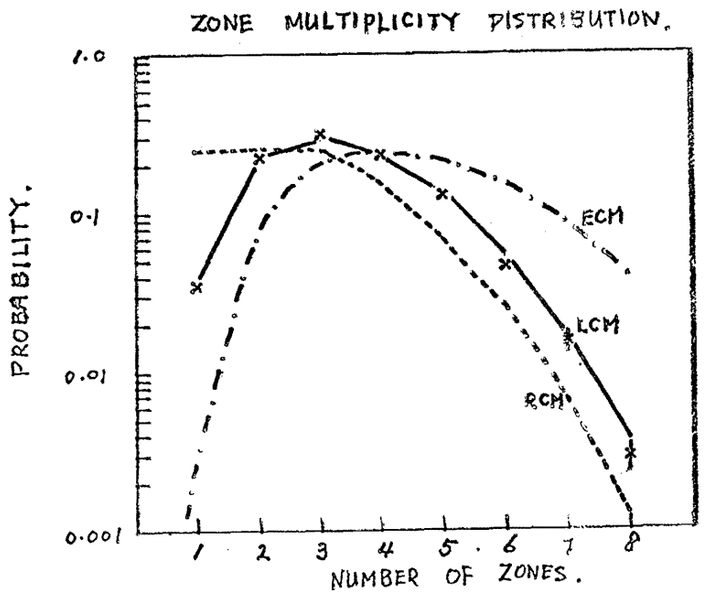

FIGURE 34

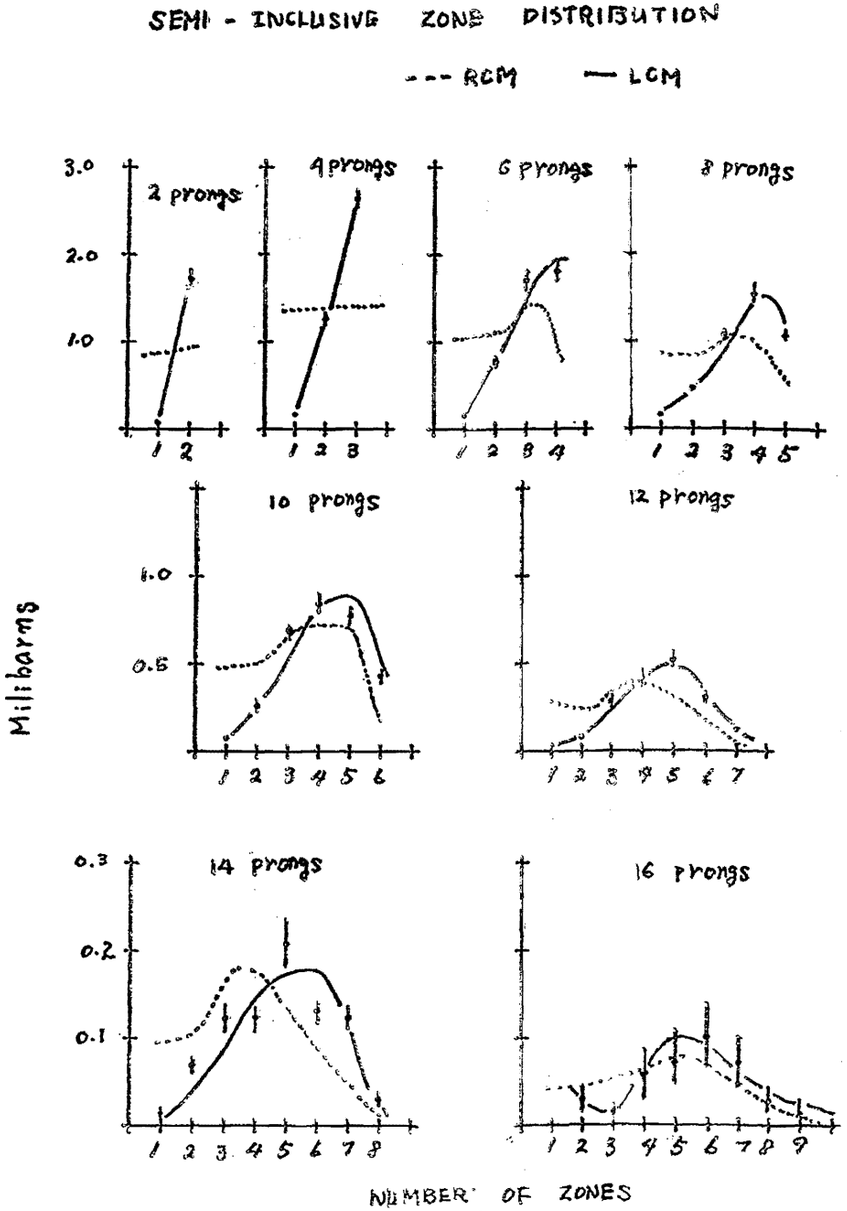

FIGURE 35

CHARGE ASYMMETRY

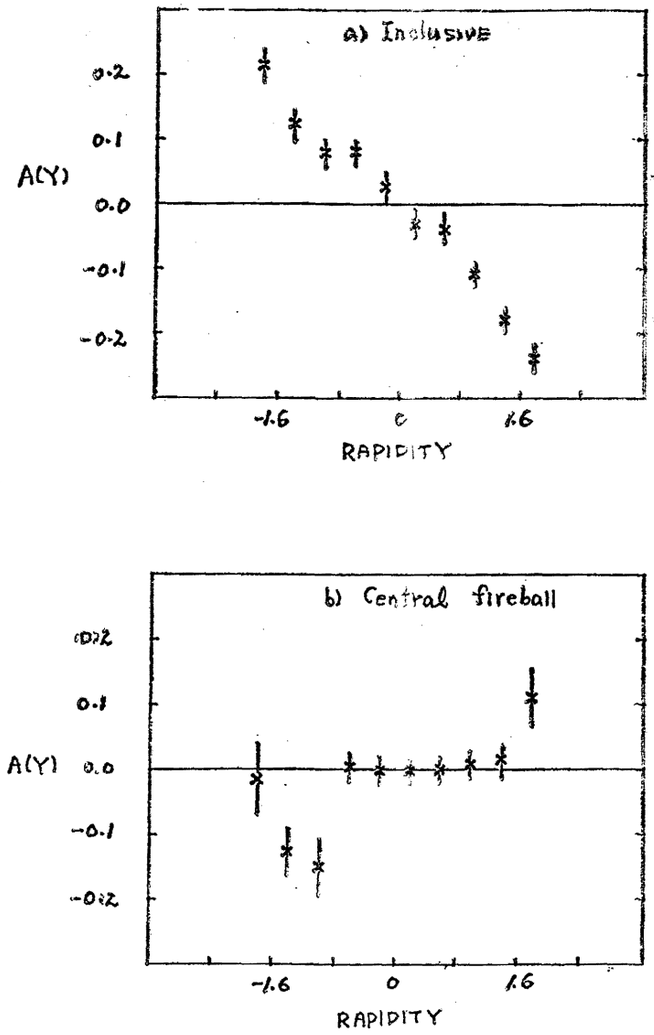

FIGURE 36

$\pi^+ p$ MOMENTUM DISTRIBUTION.

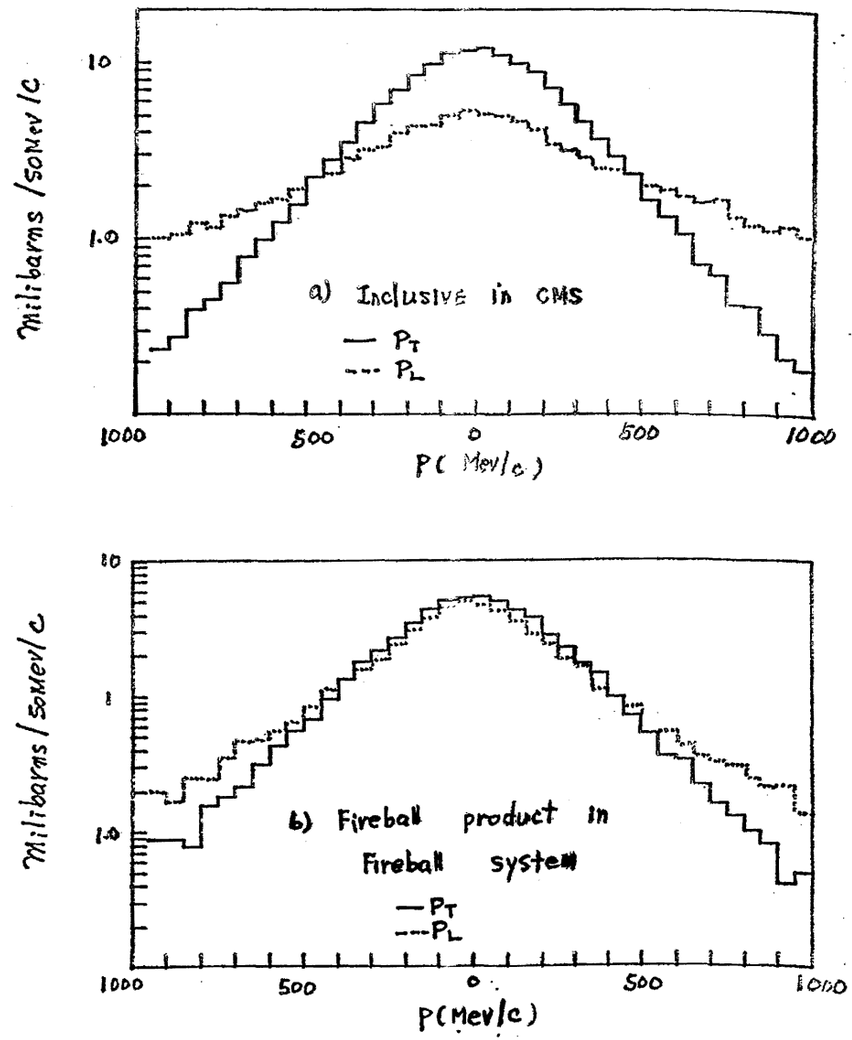

FIGURE 37

ANGULAR DISTRIBUTION OF FIREBALL PRODUCTS

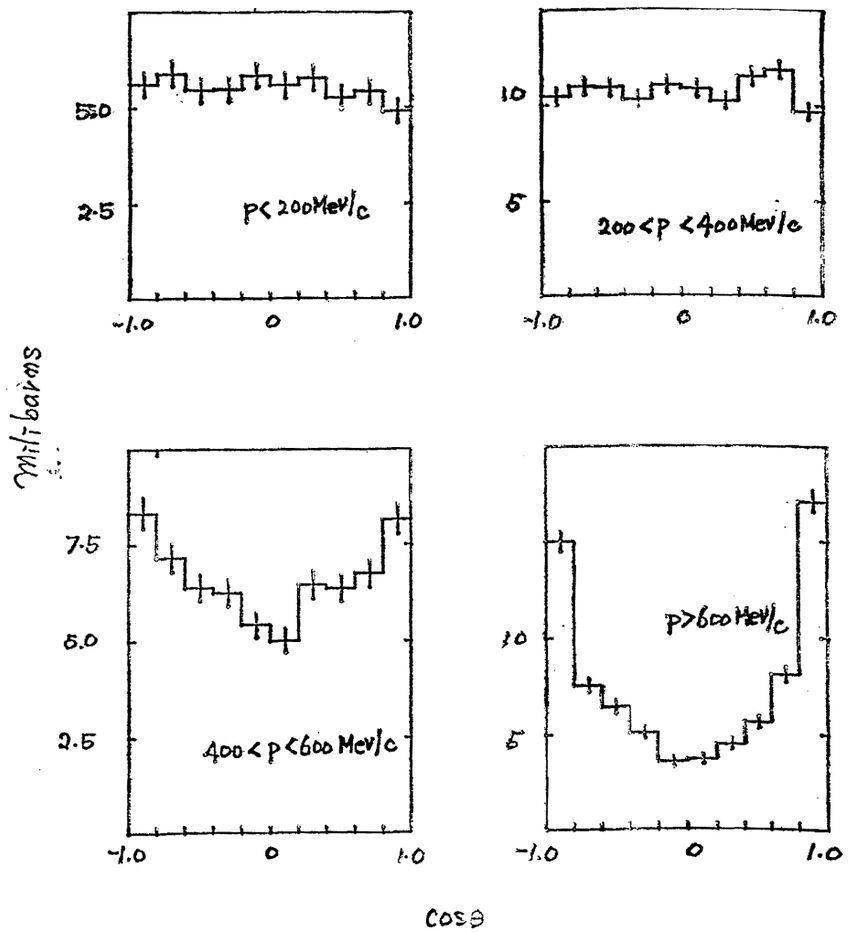

FIGURE 38

MOMENTUM DISTRIBUTION IN FIREBALL

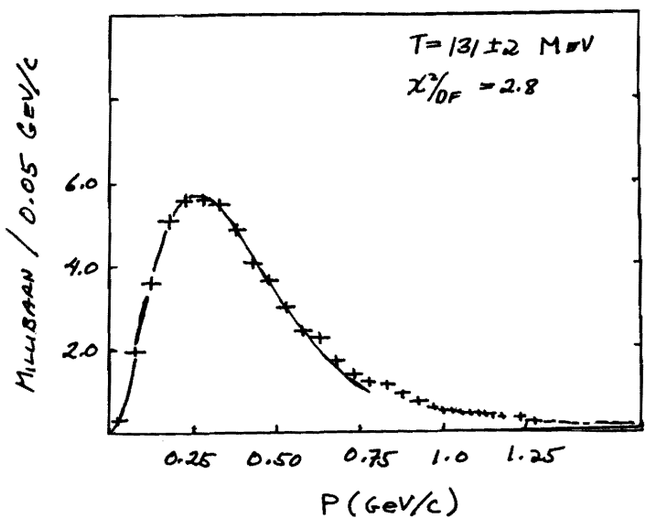

FIGURE 39